International Journal of Nanomedicine

Dovepress
Taylor & Francis Group

Open Access Full Text Article

ORIGINAL RESEARCH

Gelatin/Poly (Lactic-Co-Glycolic Acid)/Attapulgite Composite Scaffold Equipped with Teriparatide Microspheres for Osteogenesis in vitro and in vivo

Zhenrui Zhao[1], Xiaofei Feng[1], Yuhao Zhao[1], Zhengdong Song[1], Ruihao Zhang[1], Kui Zhang[1], Yixiang He[1], Guoliang Chen[1], Jing Zhang[2], Wenji Wang[3]

[1]Department of Orthopedics, The First Clinical Medical College of Lanzhou University, Lanzhou, People's Republic of China; [2]Department of Orthopedics, Anlu People's Hospital, Anlu, People's Republic of China; [3]Department of Orthopedics, the First Hospital of Lanzhou University, Lanzhou, People's Republic of China

Correspondence: Wenji Wang, The First Hospital of Lanzhou University, Lanzhou, 730000, People's Republic of China, Tel +8613893221698, Email wwjldyy@163.com

Background: Given the risks associated with autologous bone transplantation and the limitations of allogeneic bone transplantation, scaffolds in bone tissue engineering that incorporate bioactive peptides are highly recommended. Teriparatide (TPTD) plays a significant role in bone defect repair, although achieving controlled release of TPTD within a bone tissue engineering scaffold remains challenging. This work reports a new approach for treatment of teriparatide using a water-in-oil-in-water (w/o/w) microspheres be equipped on gelatin (GEL)/Poly lactic-glycolic acid (PLGA)/attapulgite (ATP) scaffold.

Methods: In this study, TPTD microspheres were prepared by the water-in-oil-in-water (w/o/w) double emulsion technique and GEL/PLGA/ATP composite scaffolds with different setups were prepared by salt leaching method. Both microspheres and scaffolds underwent physicochemical characterization. Mouse bone mesenchymal stem cells (BMSCs) were co-cultured with extracts from the microspheres and scaffolds to evaluate cell proliferation and osteogenesis. Four weeks post-implantation, the effectiveness of the scaffolds containing microspheres for repairing skull defects in mice was assessed.

Results: Both TPTD microspheres and the GEL/PLGA/ATP scaffold significantly enhanced the proliferation and osteogenic differentiation of BMSCs. Markers of osteoblast activity, including COL1, RUNX2, OCN, and OPN, were markedly up-regulated. Further, micro-CT, histological, and immunohistochemical analyses revealed extensive new bone formation on the scaffold.

Conclusion: The GEL/PLGA/ATP composite scaffold, equipped with TPTD microspheres, demonstrates significant potential for use in bone tissue engineering, providing an effective option for bone regeneration and repair in clinical applications.

Keywords: teriparatide, microsphere, gelatin, PLGA, attapulgite, bone tissue engineering, bone defect, bone regeneration

Introduction

Bone defects present a significant challenge for orthopedic surgeons. The presence of a bone defect can compromise the integrity and function of the bone, potentially leading to complications such as fracture nonunion, joint dysfunction, pain, and other symptoms.[1,2] Bone transplantation remains the primary treatment strategy for addressing bone defects. This involves the implantation of autogenous, allogeneic, or artificial bone into the defect area,[3] providing both osteogenic effects and structural support for bone repair.[4]

Autologous bone transplantation, sourced from the patient, matches the structure and composition of surrounding bone tissue, facilitating a seamless integration and offering excellent biocompatibility, osteoconductivity, and osteoinductivity.[5] However, the availability of autologous bone is limited, and the procedure may heighten the risk of additional blood loss, trauma, and infection. Conversely, allogeneic bone transplantation is costly and carries potential clinical risks including immune rejection and disease transmission.

Received: 8 September 2024
Accepted: 8 January 2025
Published: 13 January 2025

Graphical Abstract

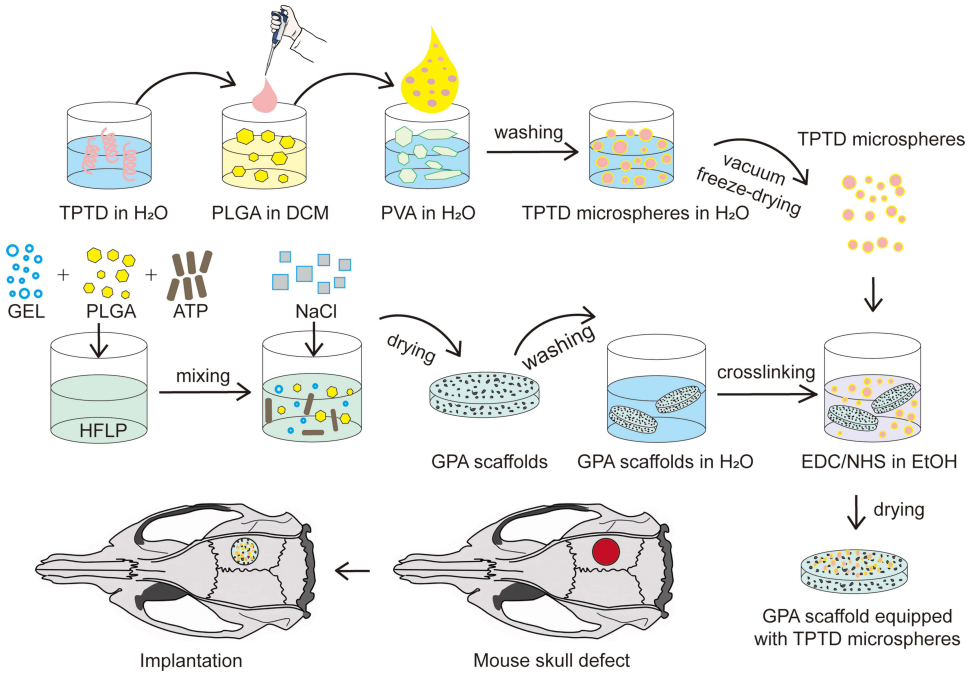

Advancements in technology have notably propelled the research and application of tissue engineering materials.[6] An ideal bone graft material should possess the following characteristics to ensure effective and safe bone defect repair: (1) good biocompatibility; (2) osteoconductivity and osteoinductivity; (3) adequate mechanical support; (4) biodegradability; (5) readily available and easy to prepare; (6) low immunogenicity and toxicity; (7) clinical adaptability and personalization.[7]

One emerging perspective in tissue engineering research involves the synergistic use of biomaterials and pharmacological agents to facilitate tissue repair.[8] Teriparatide, a parathyroid hormone analog, uniquely activates both osteoclasts and osteoblasts, balancing bone resorption and regeneration to maintain optimal bone health.[9] Evidence from several studies indicates that targeted, intermittent injections of teriparatide can effectively repair bone defects.[10,11] For enhanced delivery, encapsulating teriparatide in polymer microspheres offers a controlled release mechanism.

Poly lactic-glycolic acid (PLGA) is a biodegradable polymer noted for its excellent biodegradability, biocompatibility, film-forming ability, and sphericity.[12] PLGA, widely utilized in drug delivery, transports proteins, peptides, DNA, and various anticancer drugs.[13] Beyond drug transport, PLGA has been fashioned into a porous material conducive to osteoblast growth, demonstrating significant in vivo success in repairing full-thickness bone defects with mesenchymal stem cells (MSCs).[2] MSC proliferation and extracellular matrix (ECM) synthesis have also been noted in vitro on PLGA stents.[14] However, PLGA's hydrophobic nature presents challenges, including poor hydrophilicity, cellular affinity, and local inflammatory responses due to acidic degradation products.[15] Alone, PLGA scaffolds do not provide the mechanical strength required for guided bone regeneration (GBR) and fail to replicate the topological features of collagen and other ECM proteins found in natural cartilage. Integrating a hydrophilic polymer with PLGA to create composite scaffolds could enhance cell adhesion and functionality.[16]

Gelatin (GEL), a water-soluble biopolymer, exhibits excellent biocompatibility, hydrophilicity, biodegradability, affordability, and low immunogenicity, thus creating a conducive environment for cell nutrition, growth, and metabolism, as well as enhancing the surface hydrophilicity of PLGA.[17,18] Derived from the irreversible hydrolysis of collagen's triple helix structure through thermal and enzymatic denaturation, gelatin forms irregular, coiled domains.[19] Consequently, its molecular structure closely resembles that of collagen. Given that collagen is the primary organic component of bone matrix, gelatin can mimic and substitute collagen's biological functions. Gelatin contains amino groups that can cross-link with carboxyl-modified

PLGA to form stable amide bonds, thereby increasing the polymer's rigidity, toughness, stability, and biocompatibility, making it more suitable as a structural material.[20,21]

Physical qualities necessary for bone tissue engineering (BTE) are possessed by attapulgite (ATP), a rod-shaped crystal mineral with a nano-scale hydrated magnesium silicate structure.[22] In addition to promoting osteoblast differentiation in vitro, ATP/polymer composite scaffolds support successful in vivo bone repair and offer improved mechanical durability, according to recent studies.[23]

Despite existing research on gelatin and PLGA composites in biomaterials,[24,25] studies on ATP-doped polymer composites remain sparse, and no polymer scaffold equipped with teriparatide microspheres has been utilized for bone defect repair before. This study prepared teriparatide microspheres and gelatin/PLGA/attapulgite composite scaffolds with different setups, achieving chemical cross-linking both between the microspheres and scaffolds, and within the gelatin and PLGA components of the scaffolds. The aim was to evaluate the impact of different components of the gelatin/PLGA/attapulgite scaffolds loaded with teriparatide microspheres on bone defect repair.

Materials and Methods

Preparation of TPTD Microspheres

An water-in-oil-in-water (w/o/w) double emulsion approach was employed for the synthesis of microspheres.[26] Initially, the control batch comprised 500 μL of double-distilled water (blank microsphere, BMP), while the teriparatide batch contained 500 μL of a 100 μM teriparatide (Meilunbio, Dalian, China) aqueous solution (teriparatide microsphere, TMP). Using a tip sonicator set to 15 W for 10 seconds in an ice bath, this solution was emulsified in 5 mL of a 10% PLGA (lactide to glycolide ratio of 50:50, carboxyl-terminated, molecular weight 80 kDa, Daigang Biomaterial, Jinan, China) solution in dichloromethane (DCM, Kaitong Chemistry, Tianjin, China), creating a primary w/o emulsion. Next, 40 mL of a 1% water-based polyvinyl alcohol (PVA, molecular weight 27 kDa, Macklin, Shanghai, China) solution was gradually mixed with this emulsion while being stirred at 600 rpm. To help the microspheres settle, the liquid was swirled at room temperature for half an hour. The next step was to pour the emulsion into a 10-milliliter centrifuge tube, spin it to remove any remaining solids, and then repeat the process five times to refill the tube with double-distilled water. Next, the finished item was vacuum freeze-dried.

Characterization of TPTD Microspheres

SEM and Particle Size Analysis

We used scanning electron microscopy (SEM) to examine the TPTD/PLGA microspheres' morphological characteristics. At room temperature, the samples were first sputtered with gold. Post-coating, the microspheres were placed on a stub and analyzed using a JEOL JSM-6701F SEM at magnifications of ×250 and ×500 and an accelerating voltage of 5.0 kV. A 90 Plus Pals laser diffraction particle size analyzer was used to find the average diameter of the microspheres.

Drafting of TPTD Standard Curve

Teriparatide solutions were prepared at 25.00, 50.00, 100.00, 200.00, and 400.00 μmol/L in double distilled water. Absorbance scanning was conducted using a Thermo Biomate 3S UV-VIS spectrophotometer from 200 to 320 nm. Absorbance values were plotted against wavelength to identify the characteristic absorption wavelength. The standard curve for teriparatide in aqueous solution was established based on absorbance measurements at this wavelength.

TPTD Loading and Encapsulation Efficiency

Dissolve 0.2g of either the blank or teriparatide microspheres in 200 μL of double distilled water and 2 mL of dichloromethane. At room temperature, the solution was first vortexed for uniform mixing, followed by centrifugation. The supernatant is then transferred into a micro-cuvette. Using a UV-VIS spectrophotometer, the absorbance at the characteristic absorption wavelength was measured to calculate the concentration of teriparatide based on the standard curve. The loading and encapsulation efficiency of teriparatide were determined using equations (1) and (2):

$$TPTD\ loading\ (w/w\%) = (amount\ of\ TPTD\ in\ microspheres / amount\ of\ microspheres) \times 100\% \quad (1)$$

 https://doi.org/10.2147/IJN.S495204

$$\begin{aligned} &Encapsulation\ efficiency\ (\%) = (actual\ TPTD\ loading / theoretical\ TPTD\ loading) \times 100 \\ &= (retained\ TPTD\ amount / initially\ loaded\ TPTD\ amount) \times 100\% \end{aligned} \quad (2)$$

Degradation of Microspheres

Microspheres, both blank and teriparatide-loaded, weighing approximately 1.0 g, were placed in separate test tubes containing 10.0 mL of double-distilled water. These tubes were then incubated at 37°C in a shaking incubator. Every three days, the samples were freeze-dried under vacuum, and their weight was recorded up to day 30. Afterwards, 10 mL of fresh double-distilled water was added, and mass loss was assessed gravimetrically. The surface morphology of the degraded teriparatide microspheres was examined using SEM at ×250 magnification and an accelerating voltage of 5.0 kV after 7 and 14 days.

In vitro TPTD Release

Microspheres, both blank and teriparatide-loaded, weighing approximately 1.0 g, were placed in individual test tubes containing 2.0 mL of phosphate-buffered saline (PBS, 0.01 M, pH 7.4). These tubes were incubated in a constant temperature shaker at 37°C. Every two days, the mixture was centrifuged, 200 μL of supernatant was transferred to a micro-cuvette, and 200 μL of fresh PBS was added. The absorbance at the characteristic absorption wavelength was measured using a UV-VIS spectrophotometer, and the teriparatide concentration was determined using the standard curve until day 30. The cumulative release rate was calculated using the following formula (3), where Q represents the cumulative release rate (%); ρ_i is the drug concentration (μg/mL) at each sampling point, m is the mass (g) of the dried microspheres, s is the drug loading, V_1 is the volume (mL) of each sampling, and V_2 is the volume (mL) of the buffer solution.

$$Q = (V_1 \times \sum \rho_{i-1} + V_2 \times \rho_i) \times 10^{-6} / (m \times s) \times 100\% \quad (3)$$

Preparation of GEL/PLGA/ATP Scaffolds

Porous scaffolds composed of gelatin, PLGA, and attapulgite (ATP, nanoparticles, 150–500 nm powder, provided by Lanzhou Institute of Chemical Physics, Chinese Academy of Sciences) were synthesized through a salt-leaching technique. Initially, a 10% (w/v) solution was formed by dissolving 1.0 g of a GEL (~250 g Bloom, D&B Biotechnology, Shanghai, China)-PLGA (lactide to glycolide ratio of 50:50, carboxyl-terminated, molecular weight 80 kDa, Daigang Biomaterial, Jinan, China) co-polymer in 10 mL of hexafluoroisopropanol (HFLP, Boer Chemistry, Shanghai, China). The GEL to PLGA ratios were adjusted to 1:2 and 2:1 by weight. To this polymer solution, nanoscale ATP particles and sodium chloride particles (250–500 μm) were added, establishing ATP concentrations at 10%, 0.1 g (G1P2A1 scaffold, GEL:PLGA:ATP mass ratio of 33:67:10; and G2P1A1 scaffold, GEL:PLGA:ATP mass ratio of 67:33:10), and 20%, 0.2 g (G1P2A2 scaffold, GEL:PLGA:ATP mass ratio of 33:67:20; and G2P1A2 scaffold, GEL:PLGA:ATP mass ratio of 67:33:20). After thoroughly mixing, the mixture was poured into silicone plate molds and dried in an oven at reduced pressure for 6–8 hours to ensure complete evaporation of HFIP and solidification of the scaffolds.

Subsequently, a cross-linking solution was prepared using 50 mL of pure ethanol, 15 mmol of 1-(3-dimethylaminopropyl)-3-ethylcarbodiimide (EDC, Bidepharm, Shanghai, China), and 7.5 mmol of N-hydroxy succinimide (NHS, D&B Biotechnology, Shanghai, China). Air-dried scaffolds were immersed in this solution at room temperature. Additional groups included scaffolds combined with 0.5 g each of blank and teriparatide-loaded microspheres, as well as scaffolds devoid of any microspheres. All were agitated at 60 rpm for 24 hours. Subsequently, the scaffolds were rinsed in double distilled water for 24 hours to remove all residual EDC/NHS and sodium chloride, changing the water every 4 hours. To confirm the complete removal of NaCl, the scaffolds were tested with 0.1% $AgNO_3$ and then dried at room temperature.

Characterization of GEL/PLGA/ATP Scaffolds

SEM and Energy Dispersive Spectrometry

The morphological analysis of the GEL/PLGA/ATP scaffolds was performed using a JEOL JSM-6701F SEM. At ambient temperature, samples were sputtered with gold before scanning electron microscopy. For more general perspectives, 20 kV images were taken, whereas 5 kV images were taken for more in-depth analysis. We used energy dispersive spectrometry (EDS) in its

uncoated form, processed with image analysis software (X-Max 80, Oxford, UK), to determine the scaffolds' elemental composition.

Water Absorption, Porosity, and Contact Angles

Water absorption properties of the scaffolds were quantified by soaking them in 0.01 M PBS at 37°C, pH 7.4. Lamellar scaffolds, 20 mm in diameter, were submerged in PBS for intervals of 5 minutes and then for 3, 6, 12, 24, and 48 hours. After each interval, the scaffolds were removed, the water was drained, and they were weighed with the following formula (4):

$$Water\ absorption\ ratio\ (\%) = (W1 - W2)/W2 \times 100\% \tag{4}$$

The weights of the scaffolds before and after soaking (W1 and W2, respectively) were recorded to calculate water uptake.

For porosity assessment, lamellar scaffolds measuring 20 mm in diameter were used. The porosity was measured using a gravimetric method with the following formula (5):

$$Porosity\ (\%) = (M2 - M3 - MS)/(M1 - M3) \times 100\% \tag{5}$$

The weight of the dry scaffold is MS, the mass of the scaffold immersed in pure ethanol is M2, and the mass of the density bottle following the delicate removal of the scaffold is M3. Here, M1 is the starting mass of the bottle filled with ethanol.

An contact angle analyzer (DSA 100, Kruss, Germany), was used to measure the angles of contact. The measurement consisted of 20 mm diameter scaffolds placed on a test plate and a droplet of deionized water, measuring 0.01 mL, applied to their surface. The angle formed was recorded after 10 seconds using video capture, providing insights into the hydrophobic or hydrophilic nature of the scaffold surfaces.

Degradation of Scaffolds

GEL/PLGA/ATP scaffolds (G1P2A1, G1P2A2, G2P1A1 and G2P1A2), each weighing approximately 1.0 g, were placed in separate test tubes filled with 10.0 mL of double distilled water and incubated at a constant 37°C in a shaker. Every three days, the scaffolds were vacuum freeze-dried, and their weight was recorded over a period of 30 days. Following each weighing, the scaffolds were reintroduced into 10 mL of fresh double distilled water. Gravimetric analysis was used to determine the weight loss. Surface morphological changes in the scaffolds after 7 and 14 days were examined using SEM at a magnification of ×250 and an accelerating voltage of 5.0 kV.

Fourier Transform Infrared Spectroscopy (FTIR)

The scaffolds' functional groups were studied with Fourier transform infrared spectroscopy (FTIR; Nicolet iS50; Thermo Scientific, USA). This analysis involved creating a pellet from a mixture of 2 mg of finely powdered scaffold material and 200 mg of potassium bromide (KBr). With a resolution of 4 cm^{-1}, 32 scans were performed for each sample to obtain infrared spectra ranging from 4000 to 400 cm^{-1}. Every scaffold type (G1P2A1, G1P2A2, G2P1A1 and G2P1A2), together with the pure gelatin and PLGA samples, underwent this process three times.

Mechanical Testing

The mechanical characteristics of the scaffolds were evaluated using various methodologies. For assessing flexural strength, scaffolds were cut into rectangular strips measuring 20 mm × 50 mm and subjected to a three-point bending test. Similarly, for tensile strength evaluations, strips of the same dimensions, 20 mm × 50 mm, were used. For determining compressive strength, the samples were shaped into 20 mm × 20 mm squares. All mechanical tests were performed using an All-purpose Electronic Tester (Adamel-Lhomargy DY-35, France), equipped with a 100-N load cell and conducted at a deformation rate of 1 mm/min, with the jaws spaced 30 mm apart.

In vitro Evaluations

Extract Preparation and Cell Culture

Blank microspheres (BMP), teriparatide microspheres (TMP), and G1P2A1, G1P2A2, G2P1A1, and G2P1A2 scaffolds were sterilized using Co^{60} and sealed for extract preparation. Materials were submerged in α-minimum essential medium (α-MEM, VivaCell, Shanghai, China) at a concentration of 0.1 g/mL within a constant temperature shaker set at 37°C for

 https://doi.org/10.2147/IJN.S495204

72 hours, adhering to the Chinese National Standard (GB/T 16886.12) protocol. Subsequently, the solutions were filtered through a 0.1 μm strainer and preserved for later use.

Primary bone mesenchymal stem cells (BMSCs) were harvested from 2-week-old Balb/c mice (Lanzhou University Experimental Animal Center, Lanzhou, China). The bone marrow was flushed out with α-MEM, which was fortified with 1% penicillin/streptomycin (VivaCell, Shanghai, China). Post-centrifugation for blood cell removal, the cells were cultured in enriched α-MEM containing 15% fetal bovine serum (FBS, VivaCell, Shanghai, China) within a 37°C and 5% CO_2 incubator. Upon reaching confluence, the cells were detached using 10% trypsin-EDTA (VivaCell, Shanghai, China) and subsequently passaged. BMSCs from the second and third passages were utilized in subsequent experiments.

Cell Proliferation

The influence of microspheres and scaffold extracts on cell proliferation was quantified utilizing the cell counting kit 8 (CCK-8, Apexbio, Houston, USA). BMSCs were plated at 3×10^3 cells per well in 96-well plates. Following cell adhesion, the initial medium was replaced with the prepared extracts. These extracts were removed after 24, 48, and 72 hours of incubation, and 100 μL of α-MEM with 10 μL of CCK-8 was added to every well. Three hours later, the plates were placed in an incubator set at 37°C. With the use of a microplate reader (Bio-Rad, California, USA), the absorbance was measured at 450 nm. Each test condition was replicated six times and each assay was performed in triplicate, using α-MEM with 10 μL CCK-8 as the control.

Fluorescence Staining

BMSCs were cultured with extracts from blank microspheres, teriparatide microspheres, and various scaffolds in confocal dishes (5×10^4 cells/dish). After 10 minutes of treatment with 0.01% Triton X-100 (Solarbio, Beijing, China), the cells were found to be permeable. After you rinsed the cells three times with PBS, you stained them with 200 μL of phalloidin (Servicebio, Wuhan, China) for 60 minutes, then counterstained them with 200 μL of DAPI (Servicebio, Wuhan, China) for three minutes. After that, you washed them three more times with PBS. The nucleus and cytoskeleton were visualized through blue and green fluorescence, respectively, in an inverted fluorescence microscope (Eclipse Ti2-E, Nikon, Japan) that was used for cell imaging.

The LIVE/DEAD staining kit (Servicebio, Wuhan, China) was used to determine the cell viability. After the extract solutions were cultured for three days, 200 μL of the LIVE/DEAD reagent was added to every dish. To distinguish between live (green) and dead (red) cells, fluorescence imaging was carried out using the identical microscope.

Alizarin Reds (ARS) and Alkaline Phosphatase (ALP) Staining

BMSCs were cultured with various scaffold extracts including blank microspheres, teriparatide microspheres, G1P2A1, G1P2A2, G2P1A1, and G2P1A2 in 24-well plates at 3×10^4 cells per well. Osteogenic induction factor was composed of 1% L-glutamine (Macklin, Shanghai, China), 0.2% L-ascorbic acid (Macklin, Shanghai, China), 1% β-sodium glycerophosphate (D&B Biotechnology, Shanghai, China) and 0.01% dexamethasone (D&B Biotechnology, Shanghai, China).

After 14 days of osteogenic induction, ALP activity was assessed using an ALP Staining Kit (Beyotime, Shanghai, China) and quantified with an ALP Assay Kit (Beyotime, Shanghai, China), with absorbance readings taken at 405 nm. Protein extraction from BMSCs was performed using RIPA buffer (Solarbio, Beijing, China) containing 1% PMSF (Beyotime, Shanghai, China), and protein concentrations were determined via a BCA Protein Assay Kit (Solarbio, Beijing, China). The optical density was standardized against the bovine serum albumin (BSA, Solarbio, Beijing, China) standard curve at 590 nm, and pNPP production levels were also measured at 405 nm.

After 21 days, the BMSCs' mineral deposition was evaluated by staining them with Alizarin Red S (Beyotime, Shanghai, China). After three washing in PBS, the cells were fixed in 75% ethanol for half an hour, and then stained with 2% Alizarin Red S for half an hour at room temperature.

Quantitative Real-Time PCR

Total RNA was obtained using Trizol (Vazyme, Nanjing, China) reagent up to day 7 of gene expression analysis, after which BMSCs were grown in 25T flasks at a density of 3×10^5 cells/flask of various treatments without osteogenic induction factor. In order to synthesize complementary DNA (cDNA), a Q RT Super Mix kit (Vazyme, Nanjing, China) was utilized. A Light-Cycler system with SYBR qPCR Master Mix (Vazyme, Nanjing, China) was used to perform quantitative real-time PCR for collagen 1 (COL1), runt-related transcription factor 2 (RUNX2), osteocalcin (OCN), and osteopontin (OPN), the runt-related transcription

factor 2. The results were shown as a fold change relative to untreated controls, normalized against β-actin expression, after gene expressions were assessed using the comparative Ct (2-ΔΔCt) method. Table 1 lists the specific primers that were utilized.

Western Blot

BMSCs were cultured in 25T flasks of various treatments without osteogenic induction factor, each flask containing 3×10^5 cells. Total protein extraction was achieved using RIPA buffer supplemented with 1% PMSF. The protein concentrations were quantified using BCA protein assay kits (Solarbio, Beijing, China), and OD readings were adjusted against a BSA standard curve at 590 nm. For protein denaturation, samples were combined with loading buffer (Epizyme, Shanghai, China) in a 1:4 ratio and heated at 95°C for 10 minutes. Proteins were then separated via SDS-PAGE (Solarbio, Beijing, China) and transferred onto PVDF membranes (Millipore, Billerica, USA). Membranes were blocked using 5% BSA at 4°C for one hour, followed by an overnight incubation at 4°C with primary antibodies at the following dilutions: rabbit polyclonal COL1 antibody (1:1000, Bioss, Beijing, China, bs-0578R), RUNX2 antibody (1:1000, Bioss, Beijing, China, bs-1134R), OCN antibody (1:1000, Abmart, Shanghai, China, TD12303), OPN antibody (1:1000, Abmart, Shanghai, China, T55333), and β-actin antibody (1:5000, Proteintech, Wuhan, China, 20536-1-AP). Subsequently, membranes were incubated with horseradish peroxidase-conjugated secondary antibodies (1:5000, Proteintech, Wuhan, China, SA00001-2) for two hours. Protein bands were visualized using an enhanced chemiluminescence (ECL) kit (Solarbio, Beijing, China), and densitometry was performed using Image J software (Bethesda, MD, USA).

In vivo Evaluations

Animal Care and Bone Defect Surgery

All experimental procedures involving animals were sanctioned by the Experimental Animal Ethics Committee of the First Hospital of Lanzhou University and followed the national standards of the People's Republic of China (Laboratory animal—Guideline for ethical review of animal welfare [GB/T 35892–2018]. Animal ethic approval number: LDYY-2024-506. Each type of scaffold was cut with a surgical knife blade to 3 mm in diameter, sealed, and sterilized with Co^{60}. 54 adult female Balb/c mice (Lanzhou University Experimental Animal Center, Lanzhou, China), approximately 8 weeks old, were allocated into nine groups: one defect control group, four groups each scaffolds loaded with blank microspheres (G1P2A1-B, G1P2A2-B, G2P1A1-B, G2P1A2-B), and four groups scaffolds loaded with teriparatide microspheres (G1P2A1-T, G1P2A2-T, G2P1A1-T, G2P1A2-T). Prior to surgical procedures, mice were anesthetized using 0.5% pentobarbital sodium at 50 mg/kg. The cranial area was disinfected with 1% iodophor disinfectant, and a 3 mm circular defect was drilled into the left parietal bone with a trephine.[27] Scaffolds were implanted according to group assignments, with no materials implanted in the control group. Surgical sites were closed in layers, and postoperative care included intramuscular penicillin (400,000U) for one week. At 4 weeks, mice were euthanized with an overdose of pentobarbital sodium (100 mg/kg) for analysis (n = 6 mice per group).

Micro-CT Analysis of Mouse Cranium

Mouse craniums were preserved in 4% paraformaldehyde at room temperature for a week. Subsequently, they were imaged using a Micro-CT scanner (SkyScan-1176, Bruker, Belgium) at settings of 90 kV and 80 μA across a 45 mm field of view to produce three-dimensional (3D) representations.

Table 1 The Specific Primers That Were Utilized for qPCR

Gene	Forward primer	Reverse primer
β-actin	5'-TCCGGCACTACCGAGTTATC-3'	5'-GATCCGGTGTAGCAGATCGC-3'
COL1	5'-AACTGGTACATCAGCCCGAAC-3'	5'-CCCTCGCTTCCGTACTCGAAC-3'
RUNX2	5'-CCTCGAATGGCAGCACGCTA-3'	5'-GCCGCCAAACAGACTCATCCA-3'
OCN	5'-TGAGGACCATCTTTCTGCTCAC-3'	5'-CTGCTTGTGACGAGCTATCAGA-3'
OPN	5'-AGCAAGAAACTCTTCCAAGCAA-3'	5'-GTGAGATTCGTCAGATTCATCCG-3'

https://doi.org/10.2147/IJN.S495204

Histological Evaluation

Once the fixing was complete, the specimens were immersed in a 10% EDTA solution to remove any remaining calcium. Sections with a thickness of 5 μm were made after each specimen was fixed in paraffin. To assess bone regeneration and tissue conditioning, these slices were histologically examined using Hematoxylin and Eosin (H&E) stains and Masson's Trichrome (MT) kits (Solarbio, Beijing, China).

Immunohistochemical Staining

After deparaffinizing the tissue slices in a gradient of ethanol solutions, they were treated for 10 minutes with 3% H_2O_2 (ZSGB-BIO, Beijing, China) to block endogenous peroxidase activity. After that, the portions were heated for 8 minutes in a pressure cooker with a 0.01M sodium citrate buffer (Servicebio, Wuhan, China) to remove any remaining antigens. A 30-minute blocking procedure was carried out at room temperature with 10% goat serum. Overnight in 0.01 M PBS, the samples were incubated with primary antibodies at 4°C. Some of the antibodies used in this study were rabbit polyclonal antibodies to collagen type I (COL1, 1:200, Bioss, Beijing, bs-0578R), RUNX2 (1:200, Bioss, Beijing, bs-1134R), osteocalcin (OCN, 1:200, Abmart, Shanghai, TD12303), and osteopontin (OPN, 1:200, Abmart, Shanghai, T55333). Upon completion of primary antibody incubation, slices were rinsed with PBS (0.01M, pH 7.4). Subsequently, they were incubated for 30 minutes at 37°C with a horseradish peroxidase-conjugated secondary antibody (ZSGB-BIO, Beijing, China), followed by further washes with PBS. Counterstaining with hematoxylin and 3.3'-diaminobenzidine tetrahydrochloride (DAB, ZSGB-BIO, Beijing, China) were used to stain the sections. Microscopic observations were conducted using an Olympus microscope, and Image J (National Institutes of Health, Bethesda, USA) software facilitated quantitative analysis.

Statistical Analyses

Data were presented as means ± standard deviations (SD). Statistical assessments were performed using GraphPad Prism version 8.0 (San Diego, CA, USA). Differences between groups were evaluated using one-way analysis of variance (ANOVA), with a significance threshold set at $P < 0.05$.

Result

Characterization of TPTD Microspheres

TPTD/PLGA microspheres demonstrated a uniformly smooth surface morphology as depicted in Figure 1A a,b. SEM images captured on the 7th and 14th days of the release test revealed morphological changes and degradation of the TPTD/PLGA microspheres (Figure 1A b–d). Particle size distribution was largely homogeneous, with over 90% of the microspheres measuring between 25.57 and 94.92 μm and an average diameter of 61.11 ± 34.71 μm (Figure 1B).

For the first week, the microspheres were agglomerated and large holes appeared on the surface (Figure 1A c) and gradually loss of mass was found. By the second week, the degradation rate increased significantly, resulting in the complete collapse of the microspheres into irregular, crumpled particles with no intact spheres remaining (Figure 1A d), this crumpling may be attributed to lyophilization. The standard curve for teriparatide concentrations at 25.00, 50.00, 100.00, 200.00, and 400.00 μmol/L showed a characteristic absorption wavelength of 281 nm (Figure 1C). The degradation curve (mass loss vs time) of TPTD/PLGA microspheres is shown in Figure 1D.

The data obtained by UV-VIS spectrophotometry were put into the above equations (1) and (2), the result revealed an encapsulation efficiency of 76.06 ± 2.36% for TPTD within the microspheres, and a TPTD loading of 0.0318 ± 0.0009%.

After a 4-days burst release (70%), TPTD was released at an total rate of 20% for the remaining 20 days (Figure 1E).

Morphology and Properties of Scaffolds

GEL/PLGA/ATP scaffolds were fabricated using a salt-leaching method and some were immersed in an ethanol solution of EDC and NHS for cross-linking, with microspheres included. SEM analysis demonstrated that scaffolds without microspheres had a porous surface morphology (Figure 2A), and microspheres adhered well to the scaffold surfaces (Figure 2B).

The degradation curves for the GEL/PLGA/ATP scaffolds is presented in Figure 3B. During the first week, microspheres remained attached to the scaffolds, but small pores were evident on both the microspheres and scaffolds

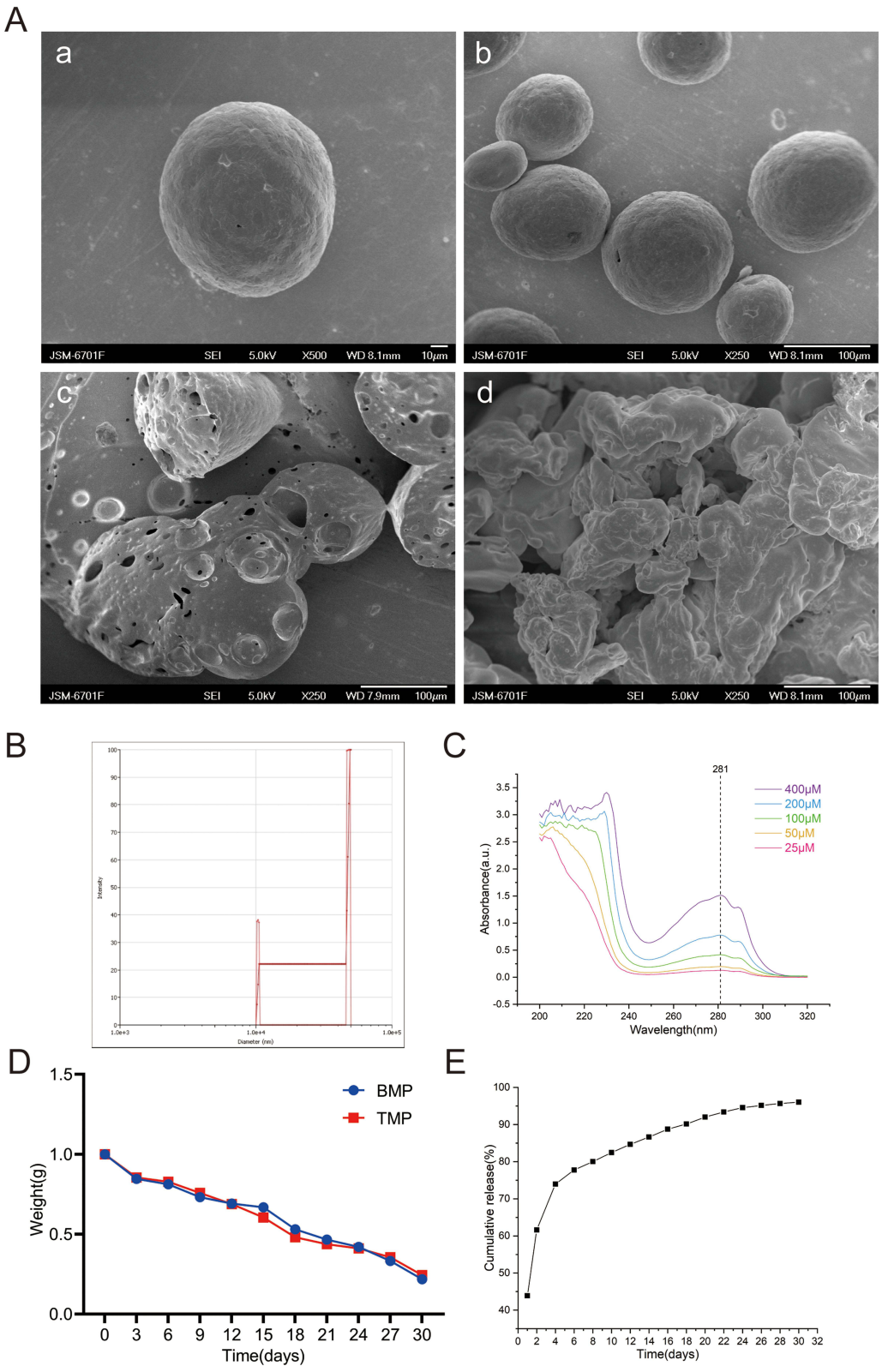

Figure 1 Characterization of microspheres. (**A**) SEM images of microspheres, (a) 0d, ×500. (b) 0d, ×250. (c) 7d, ×250. (d) 14d, ×250. (**B**) Particle size analysis of microspheres. (**C**) Absorbance curve of TPTD at various concentrations. (**D**) Degradation curves of blank microspheres (BMP) and teriparatide microspheres (TMP). (**E**) Release curve of teriparatide microspheres.

https://doi.org/10.2147/IJN.S495204

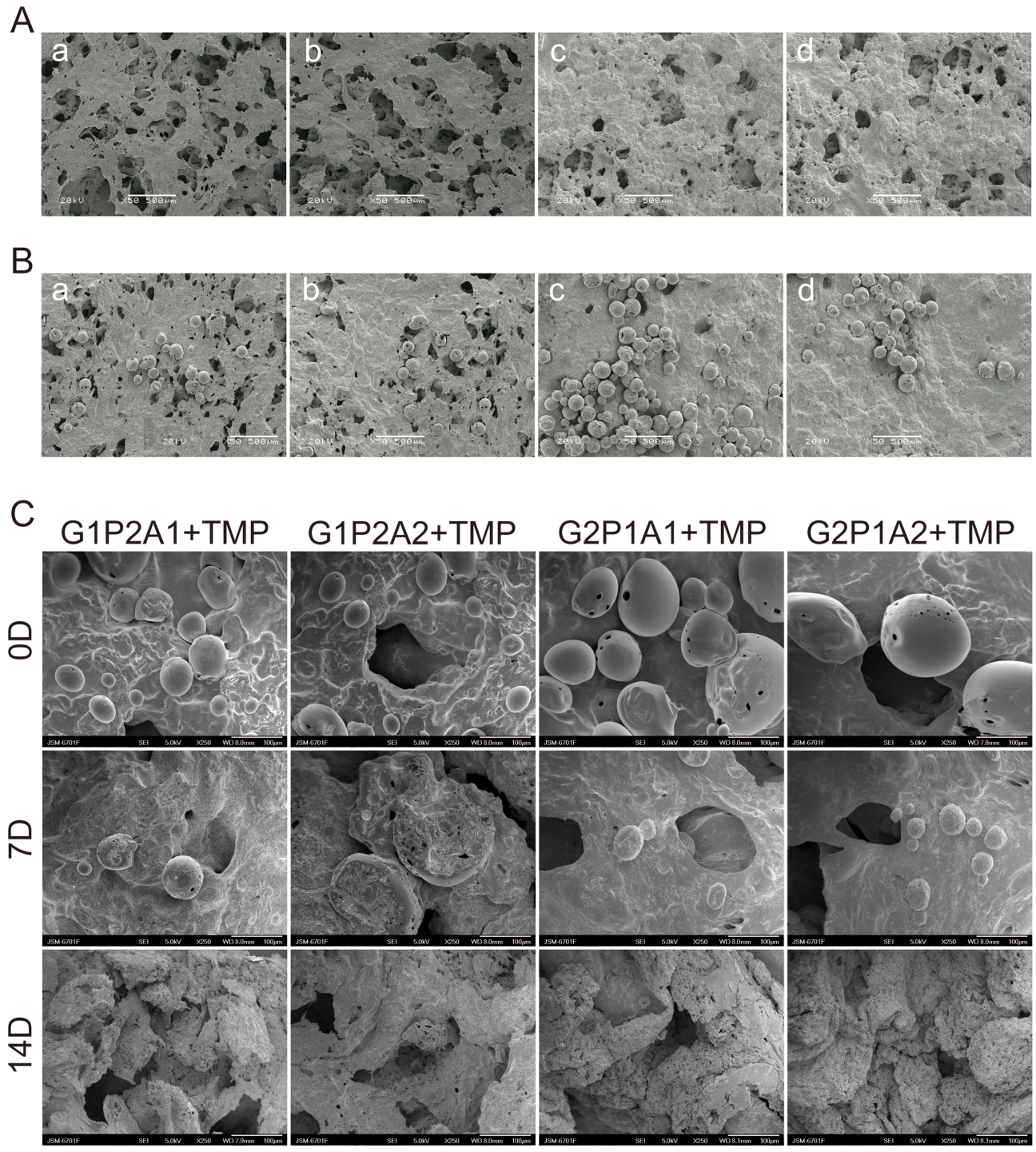

Figure 2 Morphology of scaffolds. (**A**) SEM images of scaffolds without microspheres at ×50, (a) G1P2A1. (b) G1P2A2. (c) G2P1A1. (d) G2P1A2. (**B**) SEM images of scaffolds with microspheres at ×50, (a) G1P2A1. (b) G1P2A2. (c) G2P1A1. (d) G2P1A2. (**C**) SEM images of scaffolds with microspheres at different time points at ×250.

(Figure 2C), accompanied by gradual mass loss (Figure 3B). Starting from the second week, the degradation rate increased (Figure 3B), and none of the microspheres remained attached to the scaffolds (Figure 2C), likely due to the degradation process causing the microspheres to detach.

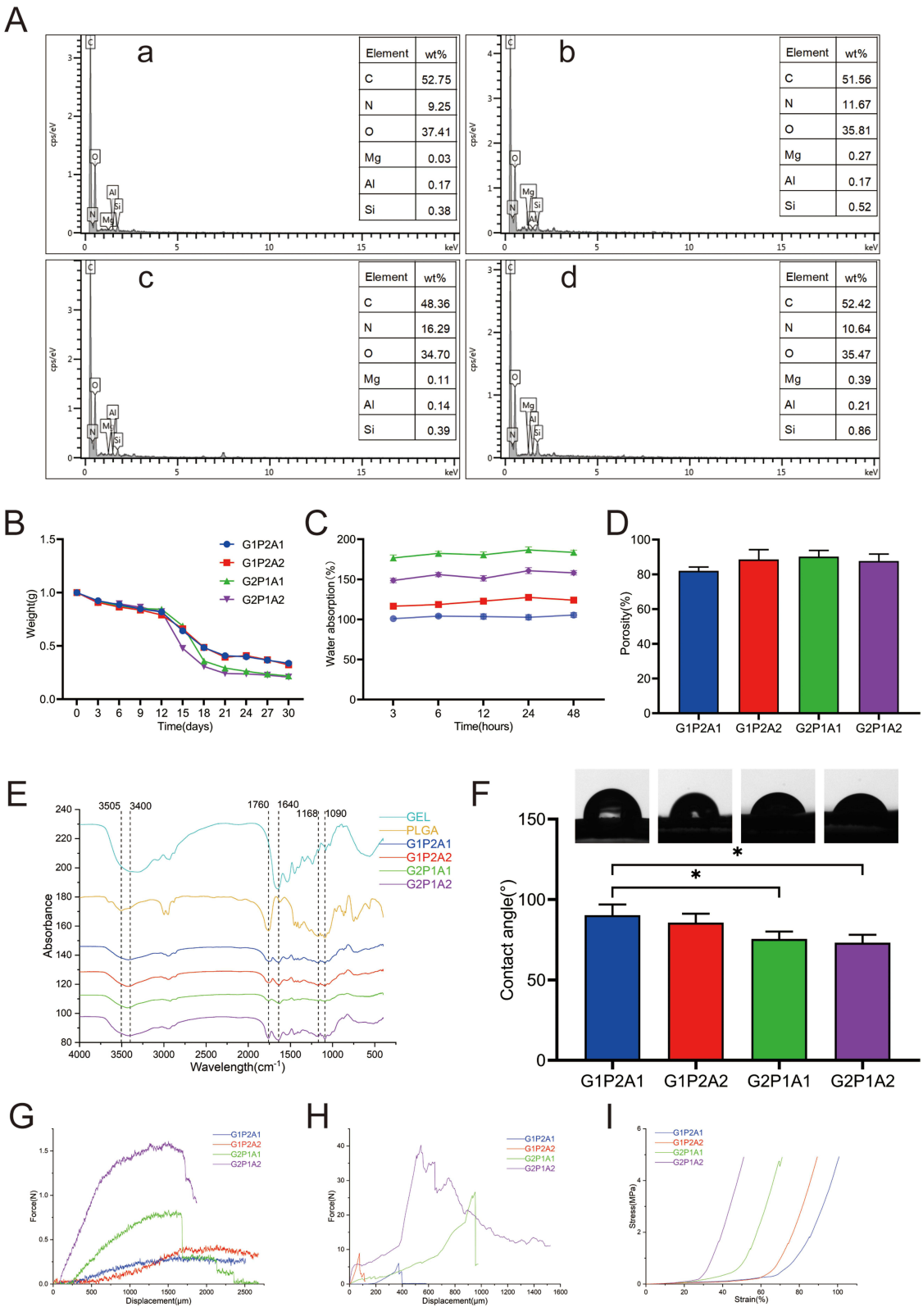

Figure 3 Characterization of scaffolds. (**A**) EDS of scaffolds, (a) G1P2A1. (b) G1P2A2. (c) G2P1A1. (d) G2P1A2. (**B**) Degradation curves of scaffolds. (**C**) Water absorption of scaffolds. (**D**) Porosity of scaffolds. (**E**) FTIR of GEL, PLGA and scaffolds. (**F**) Contact angles of scaffolds. (**G**) 3-point bending test. (**H**) Tensile strength. (**I**) Compressive strength. Data are presented as the mean ± SD (n = 3). *p < 0.05.

https://doi.org/10.2147/IJN.S495204

Physicochemical Properies of Scaffolds

Figure 3A presents the chemical composition of the GEL/PLGA/ATP scaffolds, as determined by EDS, identifying the elements C, N, O, Mg, Al, and Si. An increase in the Si element signal from 0.38% in G1P2A1 and 0.39% in G2P1A1 to 0.52% in G1P2A2 and 0.86% in G2P1A2 indicates successful doping of ATP within the scaffolds.

Water absorption data, depicted in Figure 3C, increased from 102.75% for G1P2A1 to 127.49% for G1P2A2, but decreased from 186.80% for G2P1A1 to 160.86% for G2P1A2 after 24 hours, with consistent trends at other time points, showing that both GEL and ATP are hydrophilic, though ATP has a lesser water absorption capacity than GEL.

Porosity measurements for the G1P2A1, G1P2A2, G2P1A1, and G2P1A2 scaffolds are also shown in Figure 3D. The porosity of G1P2A1 was 81.98%, increasing to 88.51% for G1P2A2. The G2P1A1 scaffold had a porosity of 90.18%, which decreased to 87.66% for G2P1A2, indicating that in the case of low gelatin content, ATP elevated the porosity, but in the case of high gelatin content, ATP decreased the porosity.

FTIR spectra of GEL, PLGA, and the GEL/PLGA/ATP scaffolds, shown in Figure 3E, indicate distinct peaks. The spectra of GEL show a typical stretching vibration peak at 1090 cm^{-1}, representing -CH_2-NH_2, which is also observed in G1P2A1, G1P2A2, G2P1A1 and G2P1A2 scaffolds but absent in PLGA. A rocking vibration peak at 1168 cm^{-1}, representing -$(CH_2)_n$-, is seen in PLGA and all types of scaffolds, but not in GEL. Peaks at 3400 cm^{-1} and 1640 cm^{-1} represent amide A and amide I from gelatinin in the G1P2A1, G1P2A2, G2P1A1 and G2P1A2 scaffolds. In PLGA and all scaffold variants, peroxy acid appear as peaks at 1760 cm^{-1}, indicative of C=O stretching vibration peaks, absent in GEL. The spectra of PLGA show a typical stretching vibration peak at 3505 cm^{-1}, representing the -OH in -COOH, which is unique in PLGA.

The water contact angles for G1P2A1, G1P2A2, G2P1A1, and G2P1A2 scaffolds are depicted in Figure 3F, showing a decrease from 90.30° in G1P2A1 to 85.66° in G1P2A2, 75.50° in G2P1A1, and 73.11° in G2P1A2. This suggests that an increased proportion of GEL and ATP enhances the hydrophilicity of the scaffolds.

The mechanical properties, such as stiffness and strength of the scaffolds, are essential for promoting bone regeneration. In 3-point bending tests, as depicted in Figure 3G, the bending modulus for G1P2A1 and G1P2A2 scaffolds was 0.25 N/2 mm and 0.35 N/2 mm respectively, while for G2P1A1 and G2P1A2, it was 0.75 N/1.6 mm and 1.5 N/1.6 mm respectively. This suggests that G2P1A1 and G2P1A2 scaffolds possess greater rigidity than G1P2A1 and G1P2A2. However, G1P2A1 and G1P2A2 scaffolds demonstrated a longer displacement at the breaking point compared to G2P1A1 and G2P1A2, indicating that while the rigidity of the scaffold increases with a higher GEL and ATP ratio, its ductility decreases. The tensile strength at breaking point was tested, as shown in Figure 3H, the tensile strength for G1P2A1 and G1P2A2 scaffolds was 6 N/0.35 mm and 9 N/0.08 mm respectively, while for G2P1A1 and G2P1A2, it was 26 N/0.9 mm and 40 N/0.5 mm respectively. The findings were analogous to 3-point bending tests results, reinforcing that an increase in GEL and ATP ratio enhances rigidity but reduces ductility in scaffolds. Additionally, compressive strength curves, illustrated in Figure 3I, reveal that when the intensity of pressure reached up to 5 MPa, the deformation of G1P2A1 and G1P2A2 scaffolds was 100% and 91% respectively. For G2P1A1 and G2P1A2 scaffolds, the deformation decreased to 71% and 51% respectively. Notably, G2P1A1 and G2P1A2 scaffolds required more force, and the slope of their curves was much steeper, indicating increased rigidity with higher GEL and ATP ratios.

Cell Viability and Proliferation Assessment

Figure 4B highlights the cellular viability and proliferation within extracts derived from the microspheres and scaffolds. BMSCs were incubated in these extracts for intervals of 24, 48, and 72 hours. Initial CCK-8 results showed no significant difference in cell proliferation on day 1, only the blank microspheres showed slight inhibition of the cells. However, on day 2, a slight increase in cell proliferation rate was observed with an increasing amount of GEL in the scaffolds, the teriparatide microsphere group increased most. By day 3, the proliferation of the G1P2A2 group became apparent, this may be related to the increasing amount of ATP in the scaffold, the teriparatide microsphere group increased most too.

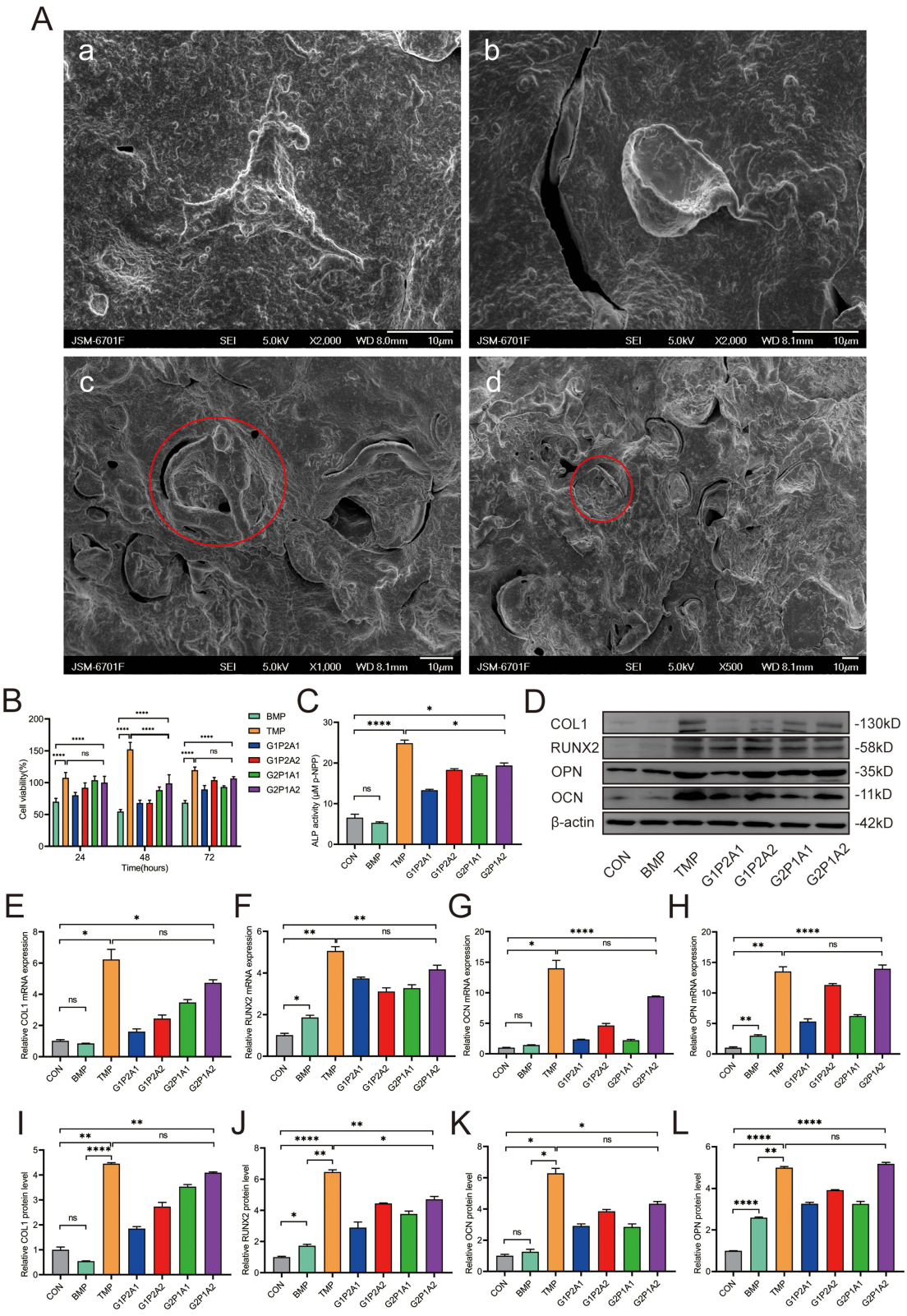

Figure 4 Biological properties of scaffolds. (**A**) SEM images of scaffolds with cells, (a, b) Cells attached onto scaffolds. (c) Cells grew into the scaffold, ×1000. (d) Cells grew into the scaffold, ×500. Red circles: cells that grew into scaffolds. (**B**) Cell proliferation assessed by CCK-8 assay. (**C**) Quantification of ALP activity. (**D**) Photograph of Western blot. (**E**) The mRNA level of COL1. (**F**) The mRNA level of RUNX2. (**G**) The mRNA level of OCN. (**H**) The mRNA level of OPN. Target genes normalized to the β-actin (n = 3). (**I**) The protein level of COL1. (**J**) The protein level of RUNX2. (**K**) The mRNA level of OCN. (**L**) The protein level of OPN. Target proteins normalized to the β-actin control band intensities (n = 3). Data are presented as the mean ± SD (n = 3). ns p>0.05, *p < 0.05, **p < 0.01, ****p < 0.0001.

https://doi.org/10.2147/IJN.S495204

Figure 4A shows the cell morphology on the different scaffolds under SEM for 2 days culture. Some cells adhered well to the surface of the scaffold (Figure 4A a,b), while others crawled into the pores of the scaffold (Figure 4A c,d).

Live/dead-stained images (Figure 5A) after 3 days of co-culture with microspheres or scaffolds extracts show well-proliferated BMSCs with few dead cells observed.

Additionally, cytoskeletal staining results are presented in (Figure 5B), showing BMSC nuclei counterstained with DAPI (blue) and F-actin fibers stained with rhodamine phalloidin (green). After 3 days of culture, BMSCs demonstrated extensive filopodia-like extensions, indicative of robust adhesion and proliferation on the scaffolds, suggesting their high biocompatibility with BMSCs.

Cell Osteogenic Property Assessment

In the ALP staining test, control group BMSCs were cultured in α-MEM with osteogenic induction factor (1% L-glutamine, 0.2% ascorbic acid, 1% β-sodium glycerophosphate and 0.01% dexamethasone). Microsphere and scaffold group BMSCs were cultured in their respective extract media with osteogenic induction factors for 14 days. Figure 5C presents the ALP staining results, showing higher activity in the TPTD microsphere group and among scaffold groups, those with a higher ATP ratio exhibited greater activity.

In the ARS staining test, similar culture conditions were used for 21 days. Figure 5C displays the results of Alizarin Red S staining, again showing higher activity in the TPTD microsphere group and among the scaffold groups with a higher ATP ratio. Additionally, staining intensity increased with higher GEL content.

The ALP quantification test reiterated these findings, with Figure 4C illustrating that the TPTD microsphere group and scaffold groups with higher ATP ratios exhibited significantly higher ALP activity than other groups after 14 days of culture in their respective extracts with osteogenic induction factors.

Expression of Osteoblast Molecular Markers

To determine the osteogenic potential of various scaffolds, the expression levels of osteogenic genes (COL1, RUNX2, OCN, and OPN) were analyzed after seven days of culturing BMSCs in extracts from different microspheres and scaffolds without osteogenic induction factor. During bone formation, COL1 encodes the α1 chain of type I collagen, contributing to bone matrix synthesis, which provides structural support and participates in bone mineralization.[28] RUNX2, a pivotal transcription factor, is crucial for osteoblast differentiation, influencing both cell proliferation and osteoblastic activity.[29] OCN, a marker of mature osteoblasts, regulates calcium ion homeostasis and bone mineralization, ensuring normal bone mineralization rates while inhibiting cartilage mineralization.[30] OPN, widely present in the ECM, is closely related to bone formation and remodeling by binding to integrin receptors on cell surfaces, thereby influencing the activity of osteoblasts, osteoclasts, and MSCs.[31]

In the RT-PCR experiment (Figure 4E–H), the expression levels of COL1, Runx2, OCN, and OPN were highest in the TPTD microsphere group. Among the scaffold groups, G1P2A2 and G2P1A2 exhibited higher expression of Runx2, OCN, and OPN compared to G1P2A1 and G2P1A1. However, COL1 expression was higher in G2P1A1 and G2P1A2 than in G1P2A1 and G1P2A2. The expression levels of these markers in the blank microsphere group were almost similar to the control group.

Western blot analysis (Figure 4D) confirmed these findings, showing similar trends in the protein levels of COL1, Runx2, OCN, and OPN to those observed in the RT-PCR experiment. Quantitative gray scale analysis (Figure 4I–L) indicated that the highest levels of these proteins were found in the TPTD microsphere group. The scaffold groups G1P2A2 and G2P1A2 showed higher expression of Runx2, OCN, and OPN than G1P2A1 and G2P1A1, while COL1 expression was higher in G2P1A1 and G2P1A2. The blank microsphere group had protein levels similar to those in the control group.

Micro-CT Measurement

The impact of GEL/PLGA/ATP scaffolds, whether containing blank or teriparatide-laden microspheres, on bone regeneration was investigated by implanting them into calvarial defects in mice for an 4-week period. The results of micro-CT plain scan and 3D reconstruction are shown in Figure 6A and B respectively. Among the tested scaffolds, the

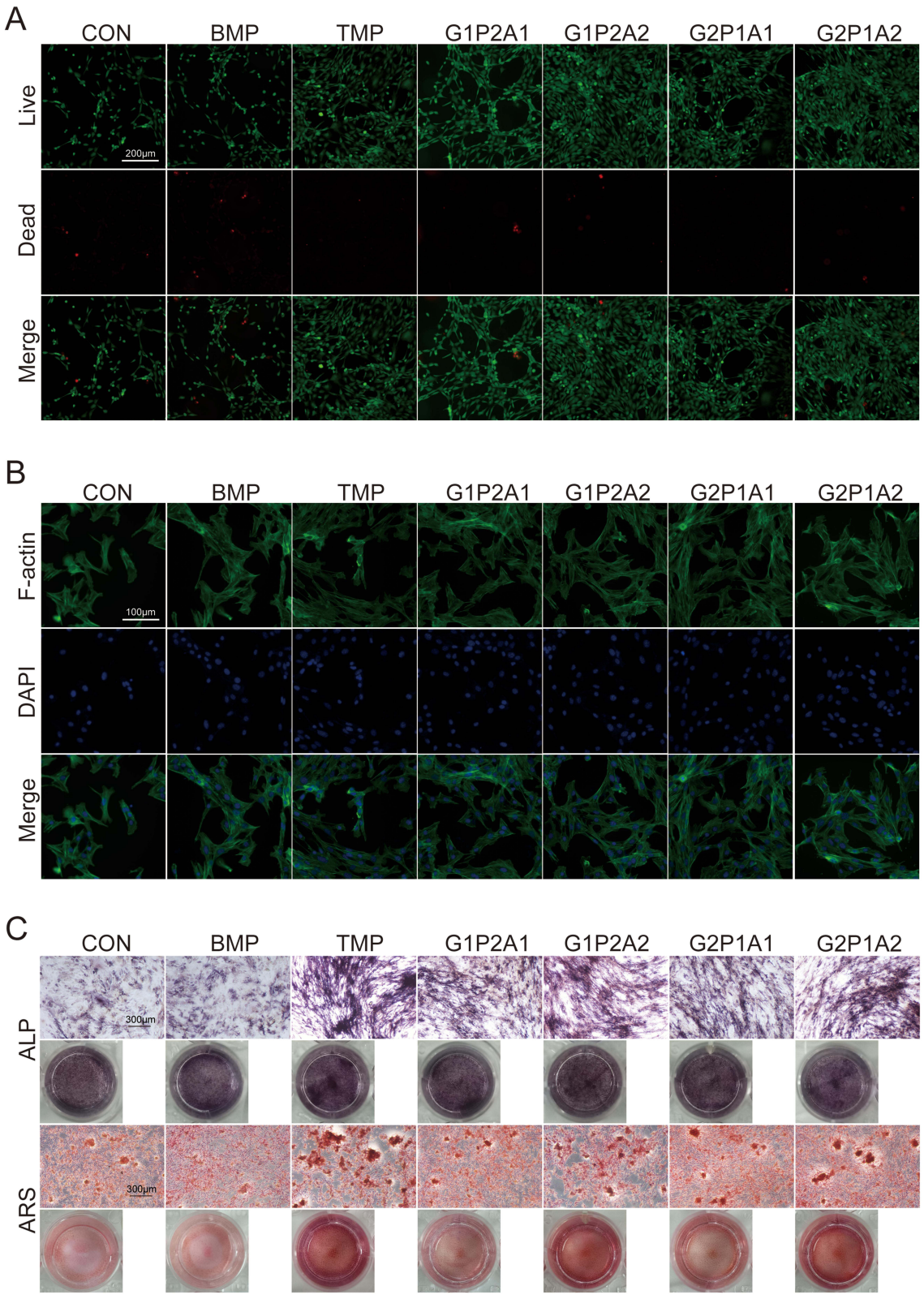

Figure 5 Staining of BMSCs. (**A**) Live/dead staining of BMSCs. (**B**) Cytoskeletal/DAPI staining of BMSCs. (**C**) ALP/ARS staining of BMSCs.

https://doi.org/10.2147/IJN.S495204

G2P1A2 scaffold equipped with teriparatide microspheres achieved the most effective bone repair, almost completely filling the defect. Sagittal views from the micro-CT scans showed that the control group largely exhibited open defects with minimal mineralization, localized at the defect's perimeter. Conversely, the G2P1A2 scaffold group displayed a markedly smaller defect area, characterized by the new mineralized tissue formation (Figure 6A and B).

Quantitative assessment of bone morphology (Figure 6C–E), including bone volume (BV), bone volume to tissue volume ratio (BV/TV), and bone mineral density (BMD), were utilized to gauge the extent of bone regeneration. After the 4-week period, BV did not show statistical significance, which may be related to the error in size when skull sampling, the BV/TV of G2P1A2-T was 12% (compared to 0.5% in the control), and the BMD of G2P1A2-T was 0.2 g/cm^3 (compared to 0.025 g/cm^3 in the control).

All scaffold groups equipped with teriparatide microspheres showed significantly higher measurements compared to their counterparts with blank microspheres. Among the different scaffold compositions, the G1P2A2 scaffold equipped with any type of microsphere exhibited superior osteogenic properties compared to the G1P2A1 scaffold with the same microspheres, and the G2P1A2 scaffold outperformed the G2P1A1 scaffold with the same microspheres. Furthermore, the G2P1A2 scaffold with any microspheres had superior osteogenic properties compared to the G1P2A2 scaffold with the same microspheres, and the G2P1A1 scaffold outperformed the G1P2A1 scaffold. These findings indicate that among teriparatide, ATP, and gelatin, teriparatide has the most positive effect on osteogenesis in bone defect repair, followed by ATP and gelatin.

Histological Analysis of Bone Regeneration

At 4 weeks post-operation, mouse calvarial tissue was excised, and new bone formation was assessed via H&E and MT staining following one month of decalcification. The H&E staining (Figure 7A) indicated an absence of inflammation across all groups, with the implanted scaffolds integrating seamlessly into the calvarial defect margin.

In the control group, the defect predominantly comprised connective tissue with scant new bone formation. Conversely, varying compositions of GEL/PLGA/ATP scaffolds, whether laden with blank or teriparatide microspheres, exhibited new bone formation at the scaffold margins. Masson staining (Figure 7B) highlighted blue-stained collagen fibers within the scaffold pores, with the extent of new bone differing across scaffold groups. Notably, quantification of the area of new bone (Figure 8B) showed the G2P1A2-T demonstrated the most substantial new bone formation.

Immunohistochemical Assessment

Immunohistochemical staining (Figure 8A) was utilized to evaluate the expression of osteogenic biomarkers COL1, Runx2, OCN, and OPN in the tissue. After 4 weeks, all groups displayed protein level expression (Figure 8C–F), were similar to trends observed in qPCR and Western blot analyses. The G2P1A2 scaffold group with TPTD microspheres exhibited the highest levels of COL1, Runx2, OCN, and OPN. Additionally, scaffolds equipped with TPTD microspheres showed higher biomarker levels compared to those with blank microspheres. Among the scaffold groups, the expression of Runx2, OCN, and OPN was elevated in G1P2A2 and G2P1A2 scaffolds containing any microspheres relative to G1P2A1 and G2P1A1 scaffolds with identical microspheres. Conversely, COL1 expression was enhanced in G2P1A1 and G2P1A2 scaffolds with any microspheres compared to G1P2A1 and G1P2A2 scaffolds. These findings suggest that both teriparatide and ATP may enhance the expression of Runx2, OCN, and OPN, whereas gelatin may preferentially boost COL1 expression.

Discussion

The ideal bone tissue engineering material should possess several characteristics: a three-dimensional porous structure, sufficient mechanical strength, machinability, plasticity, an appropriate degradation rate, safety, non-toxicity, absence of inflammatory or immune responses, excellent biocompatibility, and bone induction capabilities.[32] However, it is challenging for a single material to fulfill all these criteria, making the development of composite materials a focal point in enhancing the biological properties of materials. Both inorganic and organic graft materials offer distinct advantages and disadvantages in bone repair, and their inherent limitations restrict further application.[33] With evolving requirements for bone implant materials, synthesizing composite bone materials that amalgamate the benefits of diverse materials has become a primary objective for

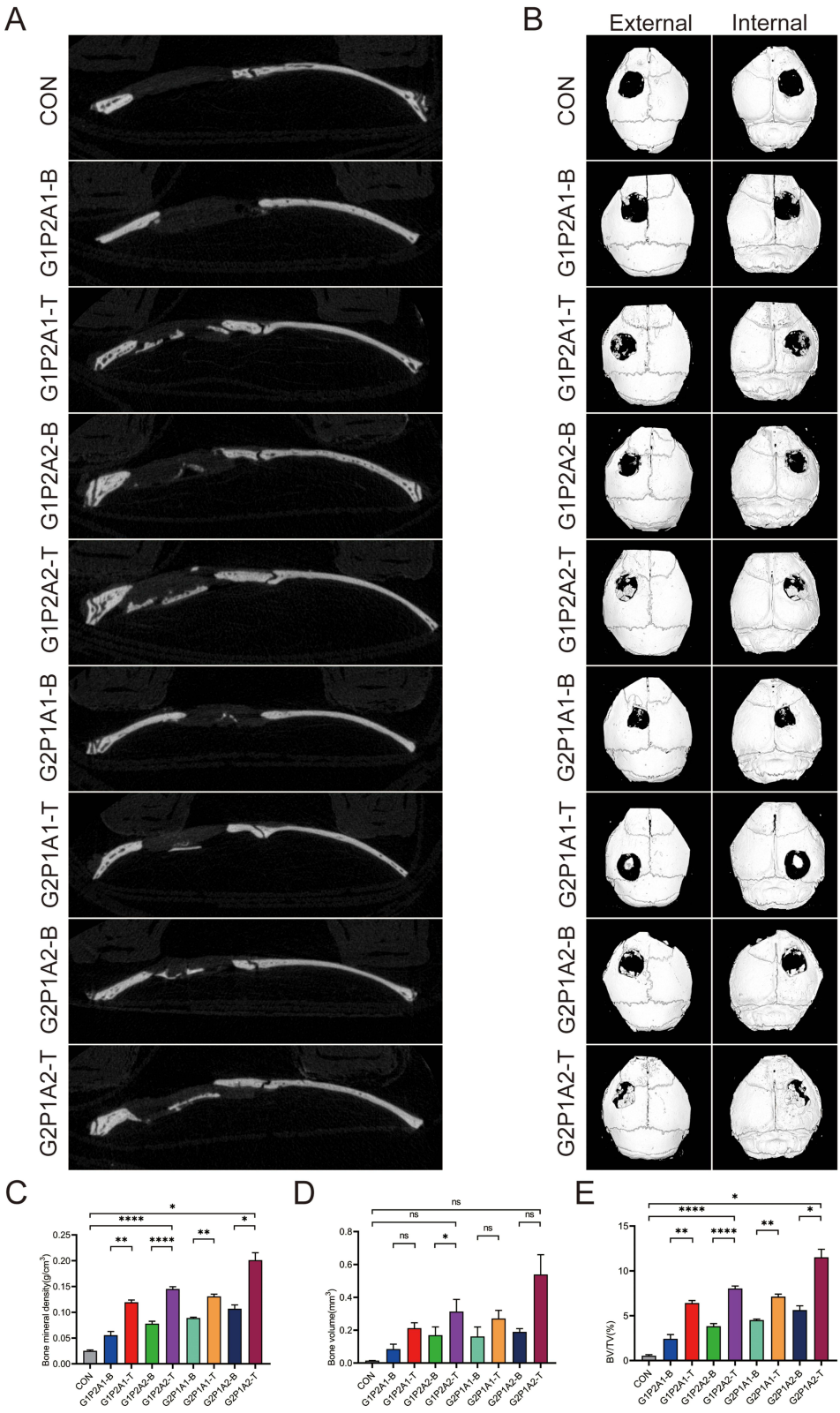

Figure 6 Micro-CT analysis of mice craniums. (**A**) Plain scan of micro-CT. (**B**) 3D reconstruction of micro-CT. (**C**) Bone mineral density (BMD). (**D**) Bone Volume (BV). (**E**) Percent bone volume/tissue volume (BV/TV). Data are presented as the mean ± SD (n = 3). ns p>0.05, *p < 0.05, **p < 0.01, ****p < 0.0001.

https://doi.org/10.2147/IJN.S495204

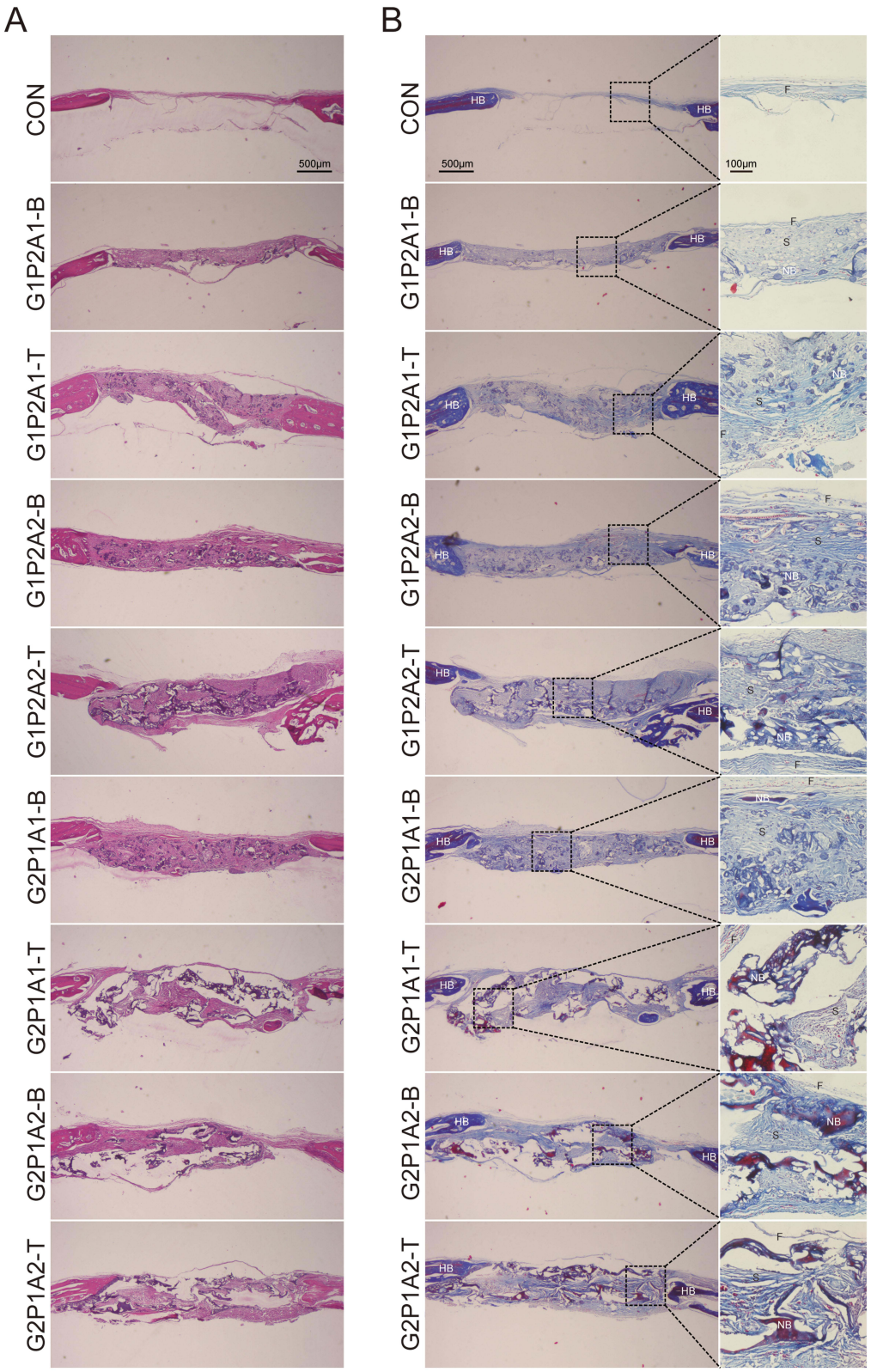

Figure 7 Histological staining results. (**A**) HE staining. (**B**) Trichrome Masson staining.
Abbreviations: NB, new bone; S, scaffold; HB, host bone; F, fibrous tissue.

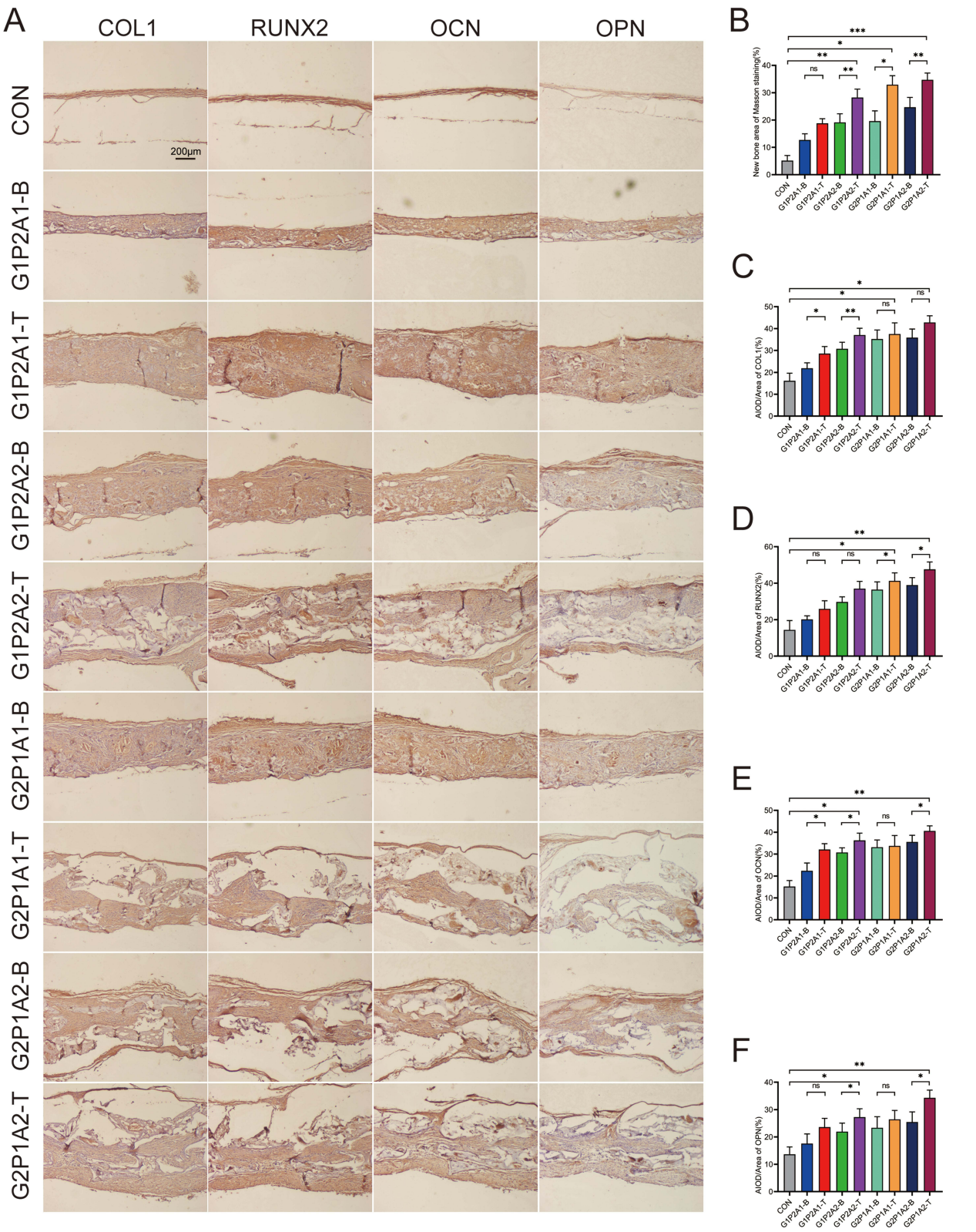

Figure 8 Immunohistochemistry assessment. (**A**) Immunohistochemistry staining. (**B**) Quantification of Trichrome Masson staining. (**C**) Quantification of protein level from COL1. (**D**) Quantification of protein level from RUNX2. (**E**) Quantification of protein level from OCN. (**F**) Quantification of protein level from OPN. Data are presented as the mean ± SD (n = 3). ns $p>0.05$, *$p < 0.05$, **$p < 0.01$, ***$p < 0.001$.

https://doi.org/10.2147/IJN.S495204

many researchers.[34,35] These composites are crafted by integrating materials with bone conduction abilities and those with inductive capacities, such as bone growth factors and trace elements, thereby significantly improving cell adhesion, proliferation, differentiation, and inducing osteogenesis to facilitate bone remodeling.

In our study, we utilized a mouse model with a 3 mm cranial defect, which represents a size incapable of spontaneous healing in mice. Moreover, our GEL/PLGA/ATP scaffolds, as polymer constructs, provide structural rigidity and load-bearing capacity, surpassing other engineering scaffolds such as hydrogels.[36] While 3D printing technology enables the production of scaffolds with more uniform pores and coaxial electrospinning yields drug-carrying scaffolds with varied polarities, both techniques require sophisticated equipment, are low in production efficiency, and incur significant time costs.[17] Conversely, the salt-leaching method allows for the rapid production of numerous bone tissue engineering scaffolds.[37] Similarly, the w/o/w double emulsion technique can swiftly produce a large volume of drug-carrying microspheres. The targeted delivery of these microspheres does not demand the same uniformity in size as those administered intravenously, reducing the risk of embolization. This presents a distinct advantage of using salt-leached scaffolds with microspheres prepared via the double emulsion technique for future clinical applications.

Teriparatide is one of the few globally approved prescriptions for promoting bone formation, boasting an impressive efficacy in reducing the risk of vertebral fractures by 65%.[38] Despite the pain and fear associated with needles, intermittent daily subcutaneous injections are recommended clinically due to the limited local bioavailability in osteoporotic bone fracture areas. Increasing the dosage can lead to significant systemic side effects, such as pronounced bone resorption and hypercalcemia, potentially causing arrhythmias and posing life-threatening risks. Achieving precise pulse release of teriparatide based on blood calcium levels remains a considerable challenge.[39,40] Extensive preclinical and clinical evidence suggests that teriparatide may hasten fracture healing, help nonunions and delayed unions, and encourage bony ingrowth in orthopedic implants; it is mainly authorized for use in the US to treat osteoporosis in postmenopausal women and men at increased risk of fracture. In 1999, researchers showed that intermittent teriparatide administration had anabolic effects on the healing of long bone fractures in a rat model of tibial fractures.[41] The volume of the fracture callus and the biomechanical strength of the mended bone are both improved by intermittent dosage of teriparatide, according to subsequent study. These effects persist even after treatment stops. In one study, scientists implanted lyophilized collagen sponges containing DNA plasmids encoding the active portion of teriparatide into critical-size tibial lesions in beagle dogs measuring up to 2.0 cm in length.[42] The results showed that 100 mg of these plasmids was required for the defect to be filled by bone, but the gap was not completely closed. Significant bone regeneration did not occur at doses between 1.0 and 20 mg, on the other hand. In a different study, the effects of daily injections of teriparatide (40 μg/kg body weight) on bone regeneration were investigated in rats with critical-size (4 mm) femoral lesions. The rats were given injections directly into the hip joint as well as had their genes delivered locally through collagen matrix. Six weeks post-operation, neither approach alone markedly increased BMD or bone mineral content (BMC) at the osteotomy site. However, the synergistic application of both systemic and localized teriparatide treatments substantially improved defect filling, as quantified by planar X-ray, compared to either method alone or untreated controls. Notably, neither study achieved complete defect filling or union. While these studies exhibit parallels with our own research, significant distinctions exist in the models used for cranial defects, methods of teriparatide delivery, the scaffolds employed, and the functional evaluation of treatment outcomes. In our study, GEL/PLGA/ATP scaffolds equipped with teriparatide microspheres exhibited exceptional osteogenic effects compared to those equipped with blank microspheres.

Gelatin, derived from irreversible hydrolysis of collagen's triple helix structure via thermal and enzymatic denaturation, forms monomolecular fibrin with random curly domains.[43] Due to its compositional and biological similarity to collagen, gelatin exhibits high biocompatibility, allowing acceptance by body cells and tissues without eliciting rejection or immune responses, thereby fostering an optimal environment for cell growth and proliferation.[44] In our study, both in vitro and in vivo assessments showed that COL1 expression was elevated in the G2P1A1 and G2P1A2 groups compared to the G1P2A1 and G1P2A2 groups, underscoring the effectiveness of gelatin in boosting type I collagen production. Similarly, Bou Assaf et al[45] developed scaffolds composed of collagen, gelatin, hydroxyapatite/tricalcium phosphate, and fibrin/thrombin, incorporating cells derived from human maxillary Schneiderian sinus membrane for application in treating defects in pig femurs. Histological analysis revealed that all three scaffolds supported new bone formation, with the gelatin scaffolds showing a more pronounced effect. Additionally, osteogenic markers COL1, RUNX-2, OCN, OPN, and ALP were significantly more abundant in the gelatin-embedded scaffolds at both two and four weeks than in other scaffolds.

PLGA is extensively used in drug delivery, medical materials, and modern industrial applications such as drug carriers and tissue engineering scaffolds due to its excellent biocompatibility, which minimizes immune rejection.[46] In vivo, PLGA degrades primarily through hydrolysis of its ester bonds, breaking down into lactic acid and glycolic acid, both of which are organic acids that contribute to the acidity of the degradation products.[47] This acidity may account for the observed inhibitory effect on the proliferation of BMSCs by blank microspheres in our study. Similarly, the inferior performance of the G1P2A1 scaffold, compared to the G1P2A2, G2P1A1, and G2P1A2 scaffolds, may be attributed to this acidity. The degradation timelines for artificial organic polymers commonly used as biomaterials are approximately as follows: 50:50 PLGA for 1–2 months; 65:35 PLGA for 3–4 months; 75:25 PLGA for 4–5 months; 85:15 PLGA for 5–6 months; DL-PLA for 12–16 months; L-PLA for over 24 months; PGA for 6–12 months; PCL for over 24 months.[48,49] Considering the typical 3–4 week healing time for mouse skulls, we selected 50:50 PLGA for our initial studies. Future research will explore scaffolds composed of polymers with varying degradation periods across different animal models and bone defect scenarios.

Attapulgite is a water-rich magnesium aluminosilicate clay mineral with a chain layer structure. It is weakly alkaline, with a pH ranging approximately from 8 to 9.[50] This alkalinity offers unique advantages in various applications; for instance, it helps regulate soil pH and enhance the soil environment for agricultural improvements, and in wastewater treatment, it facilitates the neutralization of acidic pollutants, thereby improving treatment outcomes.[51] In our GEL/PLGA/ATP scaffold, ATP effectively neutralizes the acidic metabolites of PLGA due to its weak alkalinity. Furthermore, the acid-alkaline balance of ATP is intricately linked to its surface charge characteristics, exhibiting amphoteric behavior that varies under different pH conditions. At low pH, ATP's surface carries a positive charge, enabling anion exchange capabilities. Conversely, at high pH, it is negatively charged and capable of cation exchange. Electrospinning is one of the equally excellent biological materials,[52] according to Liu et al,[23] a hydroxyapatite-doped electrospun nanomembrane with ATP displayed superior osteogenic properties compared to one doped solely with hydroxyapatite. In our research, ATP significantly enhanced the expression of osteogenic factors such as RUNX2, OCN, and OPN, a function attributable not only to its weak alkalinity but also to its rich content of magnesium ions and silicates.

The mechanical properties of scaffolds are crucial in bone tissue engineering. Our findings indicate that scaffolds with a high proportion of PLGA exhibited better ductility, whereas those with increased concentrations of GEL and ATP demonstrated greater strength. Future studies will involve adjusting the scaffold components to tailor the mechanical properties for specific applications, such as granular or structural bone grafts, to optimize bone graft suitability.

Equipping teriparatide microspheres onto GEL/PLGA/ATP scaffolds by cross-linking represents not only an innovation, but also a limitation. In this study, the microspheres were attached solely to the scaffold surface, which was suitable for the defect of the flat bone of the skull. Future research may explore the use of other types of bioceramic microspheres, such as SiO_2 or Al_2O_3, which encapsulate drugs inside the organic scaffold matrix for the treatment of long bones or irregular bones.

Conclusion

In this study, we developed a gelatin/poly(lactic-co-glycolic acid)/attapulgite composite scaffold capable of the controlled release of teriparatide to achieve the local controlled release of low-dose teriparatide, thereby fostering a conducive micro environment for bone regeneration at defect sites. Initially, teriparatide was encapsulated within PLGA and subsequently cross-linked with the GEL/PLGA/ATP scaffold. This composite scaffold effectively encouraged cell differentiation into osteoblasts and enhanced tissue regeneration through the localized release of teriparatide. Additionally, the implantation of this scaffold in cranial defect sites provided mechanical support to the local bone tissue. As the scaffold underwent swelling and degradation, the teriparatide released progressively stimulated BMSCs to enhance bone differentiation, thereby continuously augmenting local bone density and mass, which contributed to sustained protective effects.

Despite these encouraging results, it is crucial to acknowledge certain limitations of our study. Firstly, although it was established that the controlled release of teriparatide effectively stimulated osteoblast-related signaling pathways, thus facilitating bone regeneration, the precise mechanisms affecting osteoblasts and osteoclasts have not been fully delineated and require further detailed examination in the future. Secondly, the focus of this research was primarily on the short-term effects of the scaffolds on bone repair. Long-term studies are necessary to ascertain the durability of the bone formed and to investigate any prolonged effects or potential complications stemming from the scaffold materials or the degradation products

of gelatin, PLGA, or attapulgite. In addition, further dose-response studies are imperative to identify the optimal concentrations of teriparatide that maximize therapeutic advantages while minimizing adverse effects. Above all, future investigations should aim to evaluate the long-term safety, effectiveness, and feasibility of these scaffold systems.

Data Sharing Statement

The data can be obtained either through the attachment or by contacting the corresponding author.

Ethics Approval

All animal experiments received the approval of the Experimental Animal Ethics Committee of the First Hospital of Lanzhou University (Approval number: LDYY-2024-506; Date: 2024-08-28). And all experiments involving animals followed the national standards of the People's Republic of China (Laboratory animal—Guideline for ethical review of animal welfare [GB/T 35892–2018].

Acknowledgments

We would like to express our gratitude to the attapulgite provided by Prof. Aiqing Wang (Lanzhou Institute of Chemical Physics, Chinese Academy of Sciences). And extend our heartfelt thanks to Prof. Li Lin (Institute of Biochemistry, School of Basic Medical Sciences, Lanzhou University) for providing us with a research platform.

Funding

This work was generously supported by the Intramural Research Foundation of the First Hospital of Lanzhou University (ZX-62000002-2022-712).

Disclosure

The authors declare no conflicts of interest in this work.

References

1. Maruyama M, Rhee C, Utsunomiya T, et al. Modulation of the inflammatory response and bone healing. *Front Endocrinol*. 2020;11. doi:10.3389/fendo.2020.00386.
2. Park S, Heo HA, Lee K, Kim H, Pyo S. Improved bone regeneration with multiporous PLGA scaffold and BMP-2–transduced human adipose-derived stem cells by cell-permeable peptide. *Implant Dent*. 2017;26(1):4–11. doi:10.1097/ID.0000000000000523
3. Sanz-Sánchez I, Sanz-Martín I, Ortiz-Vigón A, Molina A, Sanz M. Complications in bone-grafting procedures: classification and management. *Periodontol 2000*. 2022;88(1):86–102. doi:10.1111/prd.12413
4. de Lacerda Schickert S, van den Beucken JJJP, Leeuwenburgh SCG, Jansen JA. Pre-clinical evaluation of biological bone substitute materials for application in highly loaded skeletal sites. *Biomolecules*. 2020;10(6):883. doi:10.3390/biom10060883
5. El-Rashidy AA, Roether JA, Harhaus L, Kneser U, Boccaccini AR. Regenerating bone with bioactive glass scaffolds: a review of in vivo studies in bone defect models. *Acta Biomater*. 2017;62:1–28. doi:10.1016/j.actbio.2017.08.030
6. Lee J, Byun H, Madhurakkat Perikamana SK, Lee S, Shin H. Current advances in immunomodulatory biomaterials for bone regeneration. *Adv Healthc Mater*. 2018;1801106. doi:10.1002/adhm.201801106
7. Zhang X, Chen X, Hong H, Hu R, Liu J, Liu C. Decellularized extracellular matrix scaffolds: recent trends and emerging strategies in tissue engineering. *Bioact Mater*. 2022;10:15–31. doi:10.1016/j.bioactmat.2021.09.014
8. Vermeulen S, Tahmasebi Birgani Z, Habibovic P. Biomaterial-induced pathway modulation for bone regeneration. *Biomaterials*. 2022;283:121431. doi:10.1016/j.biomaterials.2022.121431
9. Ribeiro C, Alvares L, Almeida V, et al. The local release of teriparatide incorporated in 45S5 bioglass promotes a beneficial effect on osteogenic cells and bone repair in calvarial defects in ovariectomized rats. *J Functional Biomat*. 2023;14(2):93. doi:10.3390/jfb14020093
10. Kitaguchi K, Kashii M, Ebina K, et al. Effects of single or combination therapy of teriparatide and anti-RANKL monoclonal antibody on bone defect regeneration in mice. *Bone*. 2018;106:1–10. doi:10.1016/j.bone.2017.09.021
11. Rocha T, Cavalcanti AS, Leal AC, et al. PTH1-34 improves devitalized allogenic bone graft healing in a murine femoral critical size defect. *Injury*. 2021;52:S3–S12. doi:10.1016/j.injury.2021.03.063.
12. Lei Y, Zhang QF, Kuang GZ, et al. Functional biomaterials for osteoarthritis treatment: from research to application. *Smart Med*. 2022;1(1):e20220014. doi:10.1002/SMMD.20220014
13. Wang YH, Rajalakshmanan E, Wang CK, et al. PLGA-linked alendronate enhances bone repair in diaphysis defect model. *J Tissue Eng Regen M*. 2016;11(9):2603–2612. doi:10.1002/term.2160
14. Dos Santos FP, Peruch T, Katami SJV, et al. Poly (lactide-co-glycolide) (PLGA) scaffold induces short-term nerve regeneration and functional recovery following sciatic nerve transection in rats. *Neurosci*. 2019;396:94–107. doi:10.1016/j.neuroscience.2018.11.007
15. Tendai Samkange DS, Obikeze K, Dube A, Dube A. Influence of PEGylation on PLGA nanoparticle properties, hydrophobic drug release and interactions with human serum albumin. *J Pharm Pharmacol*. 2019;71(10):1497–1507. doi:10.1111/jphp.13147

16. Mehrasa M, Asadollahi MA, Ghaedi K, Salehi H, Arpanaei A. Electrospun aligned PLGA and PLGA/gelatin nanofibers embedded with silica nanoparticles for tissue engineering. *Int J Biol Macromol*. 2015;79:687–695. doi:10.1016/j.ijbiomac.2015.05.050
17. Lee JW, Chae S, Oh S, et al. Bioessential inorganic molecular wire-reinforced 3D-printed hydrogel scaffold for enhanced bone regeneration. *Adv Healthc Mater*. 2022;2201665. doi:10.1002/adhm.202201665.
18. Rajput IB, Tareen FK, Khan AU, et al. Fabrication and in vitro evaluation of chitosan-gelatin based aceclofenac loaded scaffold. *Int J Biol Macromol*. 2022;224:223–232. doi:10.1016/j.ijbiomac.2022.10.118
19. Hsieh CF, Chen CH, Kao HH, Govindaraju DT, Dash BS, Chen JP. PLGA/gelatin/hyaluronic acid fibrous membrane scaffold for therapeutic delivery of adipose-derived stem cells to promote wound healing. *Biomedicines*. 2022;10(11):2902. doi:10.3390/biomedicines10112902
20. Rebers L, Reichsöllner R, Regett S, et al. Differentiation of physical and chemical cross-linking in gelatin methacryloyl hydrogels. *Sci Rep*. 2021;11 (1):3256. doi:10.1038/s41598-021-82393-z
21. Shabani Samghabadi M, Karkhaneh A, Katbab AA. Synthesis and characterization of electroconductive hydrogels based on oxidized alginate and polypyrrole-grafted gelatin as tissue scaffolds. *Soft Matter*. 2021;17(37):8465–8473. doi:10.1039/d1sm00118c
22. Cao L, Xie W, Cui H, et al. Fibrous Clays in Dermopharmaceutical and Cosmetic Applications: traditional and Emerging Perspectives. *Int J Pharmaceut*. 2022;625:122097. doi:10.1016/j.ijpharm.2022.122097
23. Liu J, Wu S, Ma J, et al. Polycaprolactone/gelatin/hydroxyapatite electrospun nanomembrane materials incorporated with different proportions of attapulgite synergistically promote bone formation. *Int J Nanomed*. 2022;17:4087–4103. doi:10.2147/IJN.S372247
24. Daear W, Sule K, Lai P, Prenner EJ. Biophysical analysis of gelatin and PLGA nanoparticle interactions with complex biomimetic lung surfactant models. *RSC Adv*. 2022;12(43):27918–27932. doi:10.1039/d2ra02859j
25. Ghandforoushan P, Hanaee J, Aghazadeh Z, et al. Novel nanocomposite scaffold based on gelatin/PLGA-PEG-PLGA hydrogels embedded with TGF-β1 for chondrogenic differentiation of human dental pulp stem cells in vitro. *Int J Biol Macromol*. 2022;201:270–287. doi:10.1016/j.ijbiomac.2021.12.097
26. Eswaramoorthy R, Chang CC, Wu SC, Wang GJ, Chang JK, Ho ML. Sustained release of PTH(1–34) from PLGA microspheres suppresses osteoarthritis progression in rats. *Acta Biomater*. 2012;8(6):2254–2262. doi:10.1016/j.actbio.2012.03.015
27. Marom R, Rabenhorst BM, Morello R. Osteogenesis imperfecta: an update on clinical features and therapies. *Eur J Endocrinol*. 2020;183(4):R95–106. doi:10.1530/EJE-20-0299
28. Wu XH, Downes S, Watts DC. Evaluation of critical size defects of mouse calvarial bone: an organ culture study. *Microsc Res Techniq*. 2010;73 (5):540–547. doi:10.1002/jemt.20792
29. Komori T. Molecular mechanism of Runx2-dependent bone development. *Mol Cells*. 2020;43(2):168–175. doi:10.14348/molcells.2019.0244
30. Karsenty G. Osteocalcin: a multifaceted bone-derived hormone. *Annu. Rev. Nutr.* 2023;43(1):55–71. doi:10.1146/annurev-nutr-061121-091348
31. Icer MA, Gezmen-Karadag M. The multiple functions and mechanisms of osteopontin. *Clin Chem*. 2018;59:17–24. doi:10.1016/j.clinbiochem.2018.07.003
32. McGovern JA, Griffin M, Hutmacher DW. Animal models for bone tissue engineering and modelling disease. *Dis Model Mech*. 2018;11(4). doi:10.1242/dmm.033084
33. Kim HD, Amirthalingam S, Kim SL, Lee SS, Rangasamy J, Hwang NS. Biomimetic materials and fabrication approaches for bone tissue engineering. *Adv Healthc Mater*. 2017;6(23):1700612. doi:10.1002/adhm.201700612
34. Yang C, Zhu T, Li A, et al. Porous particle-reinforced bioactive gelatin scaffold for large segmental bone defect repairing. *ACS Appl Mater Inter*. 2018;10(8):6956–6964. doi:10.1021/acsami.7b19010
35. Salehi S, Ghomi H, Hassanzadeh-Tabrizi SA, Koupaei N, Khodaei M. The effect of polyethylene glycol on printability, physical and mechanical properties and osteogenic potential of 3D-printed poly (l-lactic acid)/polyethylene glycol scaffold for bone tissue engineering. *Int J Biol Macromol*. 2022;221:1325–1334. doi:10.1016/j.ijbiomac.2022.09.027
36. Gibbs DMR, Black CRM, Dawson JI, Oreffo ROC. A review of hydrogel use in fracture healing and bone regeneration. *J Tissue Eng Regen M*. 2014;10(3):187–198. doi:10.1002/term.1968
37. Zhao H, Zhang X, Zhou D, et al. Collagen, polycaprolactone and attapulgite composite scaffolds for in vivo bone repair in rabbit models. *Biomed Mater*. 2020;15(4):045022. doi:10.1088/1748-605X/ab843f
38. Zhang L, Wang T, Chang M, et al. Teriparatide treatment improves bone defect healing via anabolic effects on new bone formation and non-anabolic effects on inhibition of mast cells in a murine cranial window model. *J Bone Miner Res*. 2017;32(9):1870–1883. doi:10.1002/jbmr.3178
39. Parameswaran R, Samuel M, Satish RL, et al. Parathyroid allotransplantation to treat post-thyroidectomy hypoparathyroidism: a review of case studies. *Surgeon*. 2021;19(3):183–192. doi:10.1016/j.surge.2020.06.008
40. Fong P, Goyal A, Brennan M, et al. Development of PTH Eluting Microspheres for the Treatment of Hypoparathyroidism. *J Bone Miner Res*. 2007;143(2):195–199. doi:10.1016/j.jss.2006.04.009
41. Andreassen TT, Ejersted C, Oxlund H. Intermittent Parathyroid Hormone (1-34) treatment increases callus formation and mechanical strength of healing rat fractures. *J Bone Miner Res*. 1999;14(6):960–968. doi:10.1359/jbmr.1999.14.6.960
42. Jacobson JA, Yanoso-Scholl L, Reynolds DG, et al. Teriparatide therapy and beta-tricalcium phosphate enhance scaffold reconstruction of mouse femoral defects. *Stem Cells Int*. 2011;17(3–4):389–398. doi:10.1089/ten.TEA.2010.0115
43. Wu DT, Munguia-Lopez JG, Cho YW, et al. Polymeric scaffolds for dental, oral, and craniofacial regenerative medicine. *Molecules*. 2021;26 (22):7043. doi:10.3390/molecules26227043
44. Guillén-Carvajal K, Valdez-Salas B, Beltrán-Partida E, Salomón-Carlos J, Chitosan CN. Gelatin, and collagen hydrogels for bone regeneration. *Polymers*. 2023;15(13):2762. doi:10.3390/polym15132762
45. Bou Assaf R, Zibara K, Fayyad-Kazan M, et al. Healing of bone defects in pig's femur using mesenchymal cells originated from the sinus membrane with different scaffolds. *Stem Cells International*. 2019;2019:1–10. doi:10.1155/2019/4185942
46. Eun Song J, Tripathy N, Rom Cha S, et al. Three-dimensional duck's feet collagen/PLGA scaffold for chondrification: role of pore size and porosity. *J Biomat Sci-Polym E*. 2017;29(7–9):932–941. doi:10.1080/09205063.2017.1394712
47. Samirah N, Setiya Budiatin A, Mahyudin F, Khotib J. Fabrication and characterization of bovine hydroxyapatite-gelatin-alendronate scaffold cross-linked by glutaraldehyde for bone regeneration. *J Physiol Pharmacol*. 2021;32(4):555–560. doi:10.1515/jbcpp-2020-0422

48. Jiang T, Petersen RR, Call G, Ofek G, Gao J, Yao JQ. Development of chondroitin sulfate encapsulated PLGA microsphere delivery systems with controllable multiple burst releases for treating osteoarthritis. *J Biomed Mater Res B*. 2011;97B(2):355–363. doi:10.1002/jbm.b.31822
49. Felfel RM, Poocza L, Gimeno-Fabra M, et al. *In vitro* degradation and mechanical properties of PLA-PCL copolymer unit cell scaffolds generated by two-photon polymerization. *Biomed Mater*. 2016;11(1):015011. doi:10.1088/1748-6041/11/1/015011
50. He L, Meng J, Wang Y, et al. Attapulgite and processed oyster shell powder effectively reduce cadmium accumulation in grains of rice growing in a contaminated acidic paddy field. *Ecotox Environ Safe*. 2021;209:111840. doi:10.1016/j.ecoenv.2020.111840
51. Jia L, Fan W, Wang P, et al. Attapulgite amendment favors the utilization of high cadmium-contaminated soil for Erigeron breviscapus cultivation. *Chemosphere*. 2023;326:138490. doi:10.1016/j.chemosphere.2023.138490
52. Xu YR, Saiding Q, Xue Z, et al. Electrospun fiber-based immune engineering in regenerative medicine. *Smart Med*. 2024;3(1):e20230034. doi:10.1002/SMMD.20230034